5-2011

Characteristics of Combustion Flame Sprayed Nickel Aluminum Using a Coanda Assisted Spray Manipulation Collar for Off-Normal Deposits

Reid S. Archibald
Utah State University

CHARACTERISTICS OF COMBUSTION FLAME SPRAYED NICKEL ALUMINUM USING A COANDA ASSISTED SPRAY MANIPULATION COLLAR FOR OFF-NORMAL DEPOSITS

by

Reid S. Archibald

A thesis submitted in partial fulfillment
of the requirements for the degree

of

MASTER OF SCIENCE

in

Mechanical Engineering

Approved:

_____	_____
Dr. Leijun Li Major Professor	Dr. Barton Smith Committee Member
_____	_____
Dr. Thomas Fronk Major Professor	Dr. Byron Burnham Dean of Graduate Studies

UTAH STATE UNIVERSITY
Logan, Utah
2011

ABSTRACT

Characteristics of Combustion Flame Sprayed Nickel Aluminum Using a Coanda Assisted Spray Manipulation Collar for Off-Normal Deposits

by

Reid S. Archibald, Master of Science

Utah State University, 2011

Major Professor: Dr. Leijun Li
Department: Mechanical and Aerospace Engineering

A novel flame spray collar called the Coanda Assisted Spray Manipulation collar (CSM) has been tested for use on the Sulzer Metco 5P II combustion flame spray gun. A comparison study of the stock nozzle and the CSM has been performed by evaluating the porosity, surface roughness, microhardness, tensile strength and microscopy of normal and off-normal sprayed NiAl deposits. The use of the CSM collar resulted in the need to position the sprayed coupons closer to the gun, which in turn affected the particle impact energy and particle temperatures of the NiAl powder. For the CSM, porosities had a larger scatterband, surface roughness was comparably the same, microhardness was lower, and tensile strength was higher. The microscopy analysis revealed a greater presence of unmelted particles and steeper intersplat boundaries for the CSM. For both processes, the porosity and surface roughness increased and the microhardness decreased as the spray angle decreased.

(91 Pages)

ACKNOWLEDGMENTS

I would like to express my deepest love and appreciation to my eternal companion, Stefani, who has been my devoted companion through this thesis. This thesis belongs to her as much as it belongs to me. I would also like to thank Dr. Li who has supported this project both monetarily and academically even though he never had any obligation to do so. Finally, I would like to thank Dr. Smith for providing the beginnings for this entire adventure.

Reid Archibald

TABLE OF CONTENTS

ABSTRACT iii
ACKNOWLEDGMENTS iv
TABLE OF CONTENTS v
LIST OF TABLES vii
LIST OF FIGURES viii
INTRODUCTION TO THERMAL SPRAY 1
Motivation for Research 4
LITERATURE REVIEW 7
Splat Formation Characteristics 7
Effective Diameter 8
Circularity 8
Splashing 10
Deposit Characteristics 13
Porosity 13
Surface Roughness 21
Hardness 27
Tensile Strength 29
OBJECTIVES 32
Statement of Problem 32
Statement of Purpose 32
Statement of Need 32
METHODOLOGY 34
Statement of Conditions 34
Statement of Limitations 34
Statement of Hypothesis 34
Setup and Preliminary Calculations 34
Spray Angle Setup 40
Constant Temperature Setup 43
Time Dependent Temperature Profile and Impact Energy Calculations 43
Testing Procedures 47
Porosity Measurement 47
Surface Roughness and Profile Measurements 48
Microhardness Measurement 49
Tensile Strength Measurement 49
RESULTS AND DISCUSSION 50
Porosity Measurement 50

Surface Roughness Measurement 53
Microhardness Measurement 55
Tensile Strength Measurement 59
Microscopy 64
CONCLUSION 69
REFERENCES 70
APPENDIX 72

LIST OF TABLES

Table Page

1 Distributions For the Deposited Mass, Direction Angle, and Droplet Size [7]. 23

2 Powder Diameters 26

3 Flame Spray Parameters 35

4 Test Design Matrix 36

5 Assumed Parameters Used to Calculate the Time Dependent Temperature Profile. 44

6 Estimated Kinetic Energies 47

7 Porosity Methods 73

8 Surface Roughness Methods 74

9 Hardness Methods 75

10 Tensile Strength Methods 76

LIST OF FIGURES

Figure		Page
1	The 5P Metco II combustion flame spray gun..	2
2	A general cross-section of a flame sprayed coating.	3
3	A complex surface inhibiting thermal spraying..	4
4	A CAD model of the CSM collar.	6
5	A demonstration of how the CSM collar works.	6
6	A splat impact schematic.	10
7	Individual splat formations sprayed at various angles.	11
8	Surface roughness influence on splashing.	12
9	Porosity data plots [3,11,12].	14
10	Porosity data plots (Continued) [10].	15
11	A typical thermal spray cone zshematic.	16
12	Momentum in splat formations.	17
13	The shadow effect.	18
14	Polished and etched molybdenum sprayed at 30 degrees.	19
15	Typical microstructure of plasma sprayed ceramic deposits.	20
16	An image showing the over spray region.	22
17	The surface roughness of the spray in reference to their zones.	23
18	Surface roughness data plots[3,11].	24
19	Surface roughness data plots (continued)[10].	24
20	Surface roughness data plots (continued) [14].	25
21	Surface roughness of small diameter powders [11].	26

22 Surface roughness of small diameter powders (continued) [10]..... 27

23 Measured coating hardness [3,11,14]. 28

24 Measured coating hardness [14]. 29

25 Measured coating tensile strength [3,11]. 30

26 Spalling due to a decrease in normal momentum [8]..... 31

27 The front view of the coupon position schematic. 37

28 The coupon orientation schematic. 38

29 The cycle path schematic. 39

30 A digital image of the vectored spray and column truncation method. 42

31 Plot of the measured spray angle vs. the volumetric flow rate of the secondary gas. 42

32 Time dependent temperature profile of vectored and un-vectored Ni particle spheres for h=10,000 W/m^2 K. 47

33 Vectored porosity test results. 50

34 Un-vectored porosity test results..... 51

35 Un-vectored and vectored spray cones. 52

36 Vectored surface roughness test results. 54

37 Un-vectored surface roughness test results. 54

38 Vectored microhardness test results..... 56

39 Un-vectored microhardness test results. 57

40 Sampath microhardness study [18]. 59

41 Vectored tensile strength test results..... 61

42 Un-vectored tensile strength test results. 62

43 The surface roughnesses of the substrate surface. 64

44 Microscopy images showing the splat formations for the vectored a) and un-vectored b) processes for the 90º spray angle. 65

45 Microscopy images showing the splat formations for the vectored a) and un-vectored b) processes for the 75º spray angle. 65

46 Microscopy images showing the splat formations for the vectored a) and un-vectored b) processes for the 60º spray angle. 66

47 Microscopy images showing the splat formations for the vectored a) and un-vectored b) processes for the 45º spray angle. 66

48 Coupon dimensions. 77

49 Partial circumference collar dimensions. 78

50 Partial circumference control panel dimensions. 79

51 Insert dimensions. 80

52 Thread attachment dimensions. 81

CHAPTER 1

INTRODUCTION TO THERMAL SPRAY

The flame spray process is similar to the spray paint process except that molten metallic or ceramic material is sprayed instead of a liquid paint. A typical thermal spray gun setup consists of a gas source, a material feed source, a heat source and a nozzle (Figure 1). The gun can either be hand held or mounted to the arm of a programmable robot. The operator of the gun usually moves the gun back and forth over the surface of the sprayed object until the desired thickness is obtained. Once the desired thickness is reached the part is ready for any post processing such as heat treatment, machining, etc.

Thermal sprayed coatings are used in a variety of industries for a variety of purposes with the main driving purpose of minimizing production cost during manufacturing. Thermal spray is used to coat surfaces for industries such as automotive, defense, food processing, healthcare, and nuclear, to name just a few. These coatings are used for wear resistance, heat resistance, clearance and dimensional control, corrosion and oxidation resistance and electrical properties. Sprayed surfaces are employed to help the base part last longer and perform better [1].

Thermal sprayed coatings bond to the substrate of the object being sprayed primarily through a mechanical bonding (Figure 2). Very little if any chemical bonding must occur for the deposit to adhere. This feature allows non-similar materials to bond together such as ceramics to metals or different metals such as steel to aluminum. Another advantage is that thermal spray coatings have an extremely high cooling rate. Therefore, heat sensitive materials can be sprayed with coatings that have extremely high melting points without damaging the substrate. Thermal spray's high material deposit rate

(up to 23 kg/h) can also be used to create near net shapes. Such shapes can then be more precisely machined down to meet specified dimensions. These advantages combine to provide protection and cost savings for manufacturers of many products.

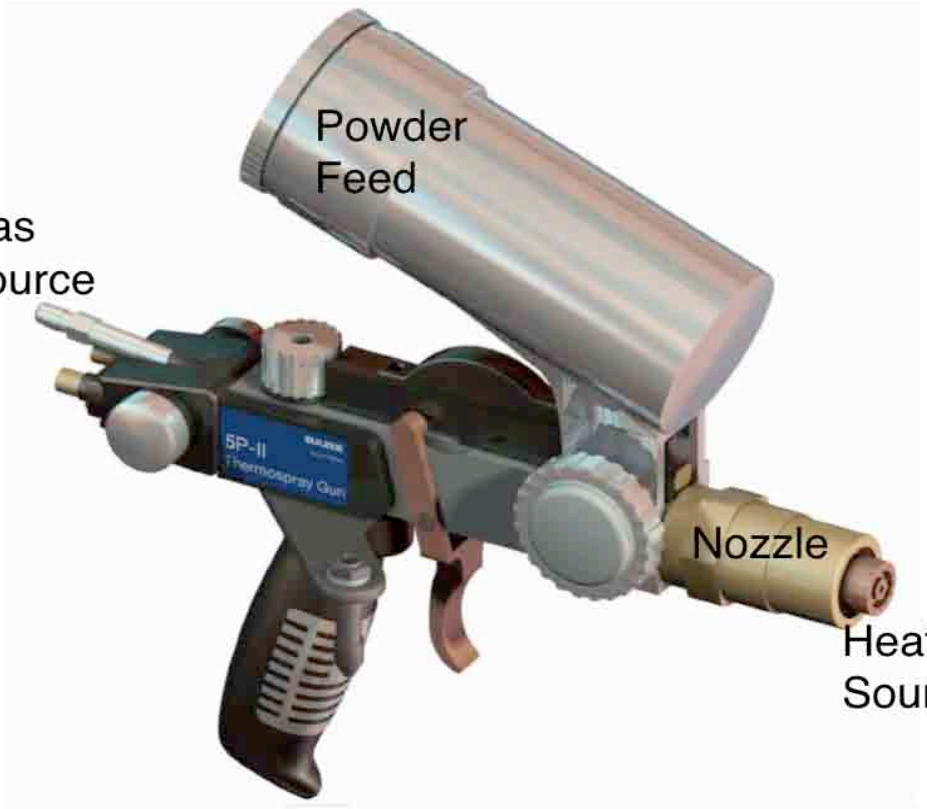

Figure 1 The 5P Metco II combustion flame spray gun. This gun was used for this experiment. Like all powder flame spray guns it has a gas source, powder feed source, a nozzle and a heat source.

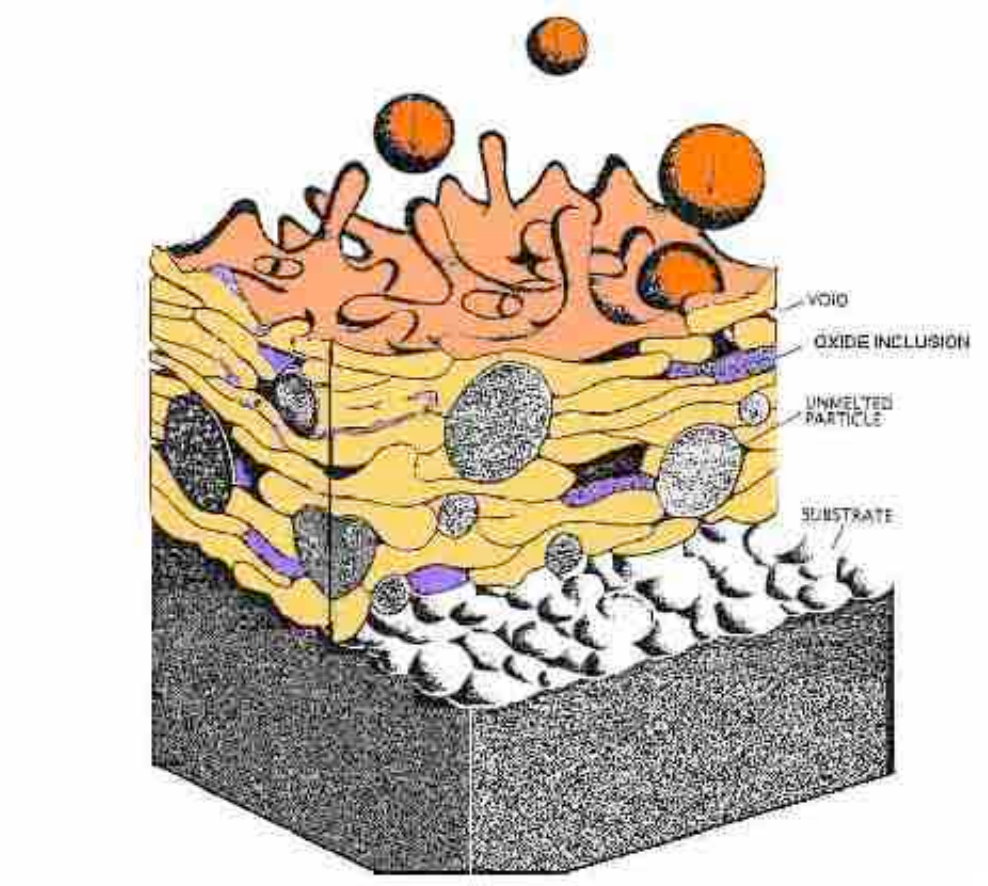

Figure 2 A general cross-section of a flame sprayed coating. It includes areas of voids, oxide inclusions, unmelted particles and the substrate [2].

Motivation for Research

One disadvantage of all thermal spray processes today is that they require that sprays must be applied nearly perpendicular to the surface being coated. Obstacles such as overhanging features and small interior dimensions can prohibit thermal spray guns and their robotic arms from accessing certain part features at an optimal angle Figure 3 When it is not possible to spray at a perpendicular angle to the surface the quality of the deposit begins to decrease in many characteristics such as porosity, surface roughness, density and tensile strength.

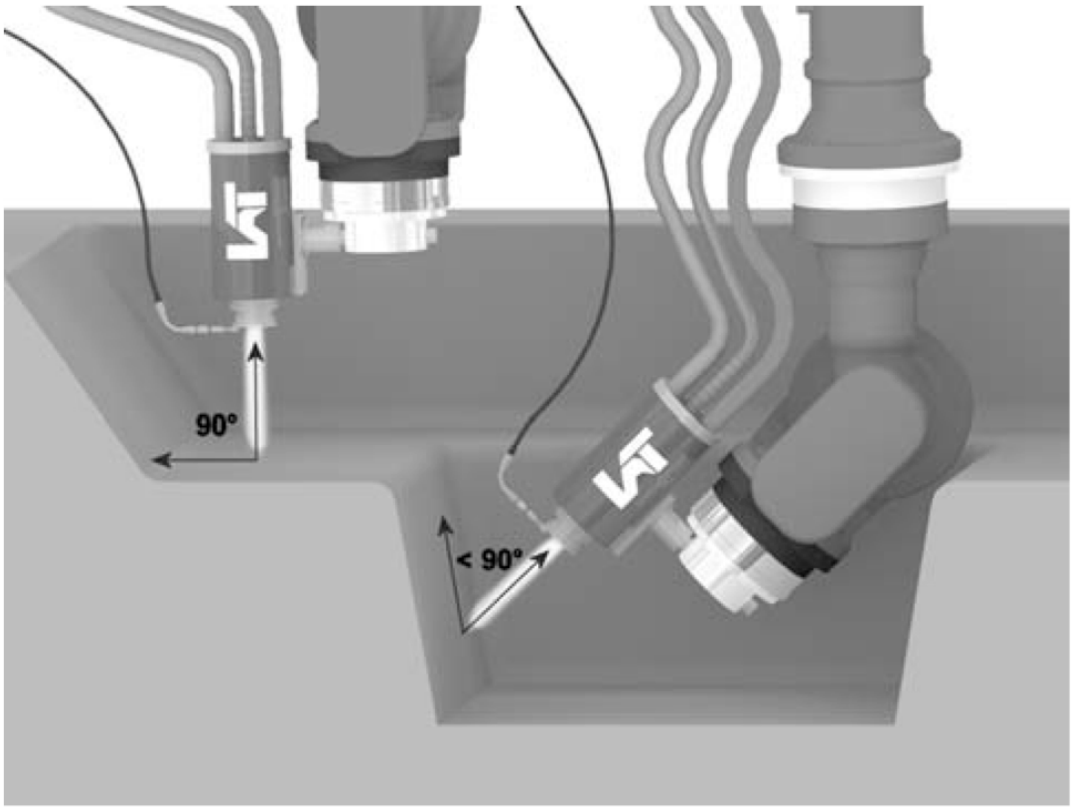

Figure 3 A complex surface inhibiting thermal spraying. This figure shows how an arbitrary part may have in-accessible surface features for coating. When the spray angle is less than 90º coating characteristics qualities begin to decrease [3].

The Coanda-Assisted Spray Manipulation (CSM) collar, a new thermal spray gun nozzle attachment, has been developed to allow thermal sprays to be vectored Figure 4. The CSM uses a secondary gas flow situated parallel to the primary flow of the thermal spray gun which entrains the primary flow into the secondary flow and then vectors the primary flow using the Coanda effect (the natural tendency of a fluid to wrap around the surface of an object it is flowing next to, like water on the convex surface of a spoon). As illustrated in Figure 5 the primary flow of the thermal spray then wraps around the convex surface of the CSM. By adjusting the mass flow rate of the secondary gas flow the angle of the primary flow can be changed. Therefore the axis of the gun can be pointed off-normal from the surface needing to be sprayed, but the primary flow could be sprayed perpendicularly to the surface. This would allow for coatings to be sprayed where it would otherwise be impossible to align the axis of the gun due to dimensional constraints. For further detail on the development and testing of the CSM the author encourages the reader to refer to [4].

The purpose of this thesis is to test and measure the deposition properties of a NiAl alloy powder deposited to off-angle substrates in order to prove the capability of the CSM collar for the combustion flame spray process.

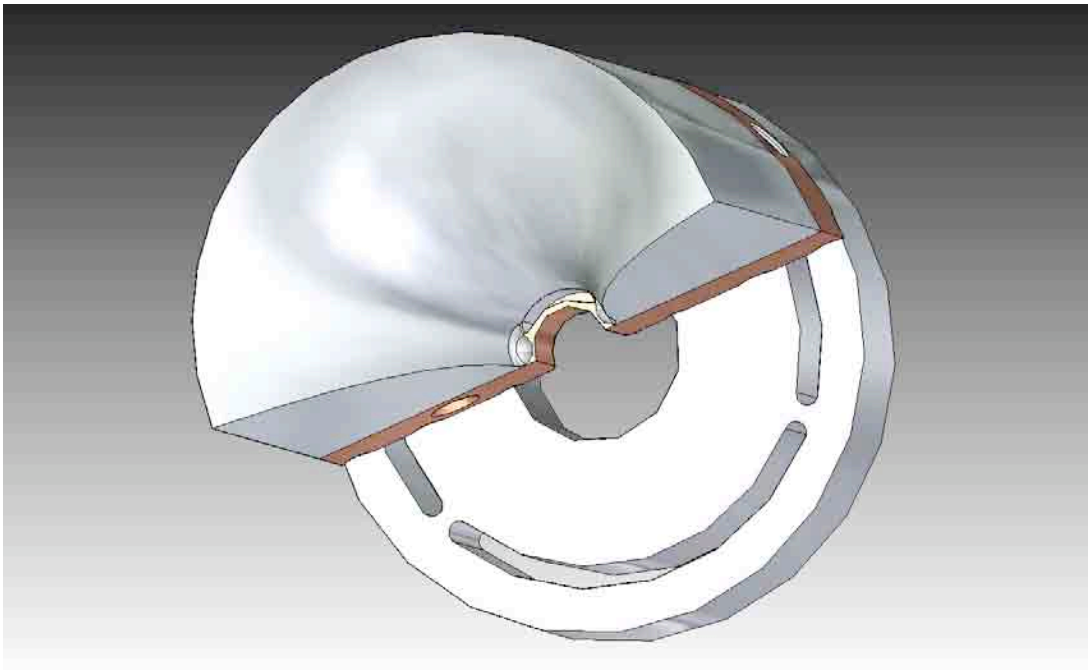

Figure 4 A CAD model of the CSM collar. This can be attached to the existing nozzle of a flame spray gun to allow for vectoring of the flame spray.

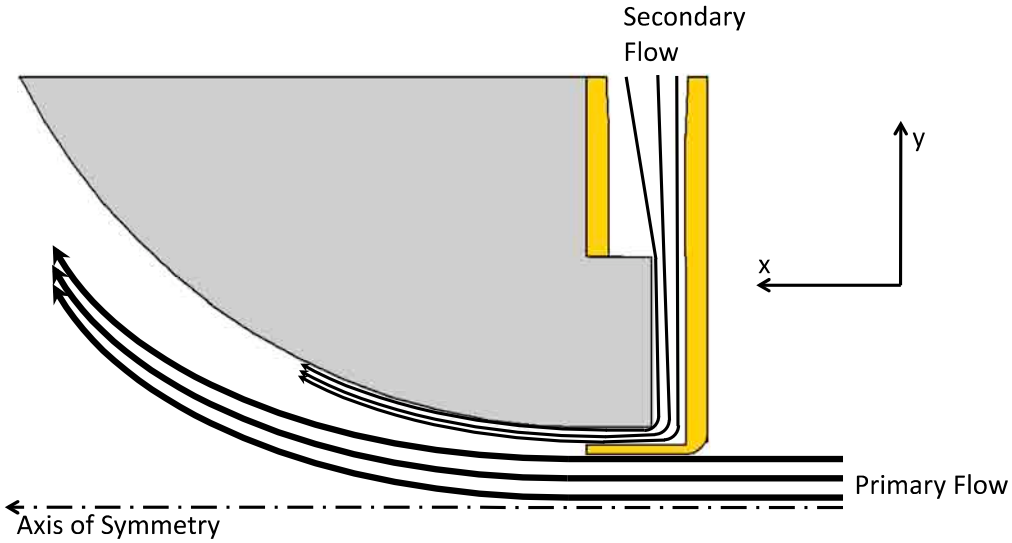

Figure 5 A demonstration of how the CSM collar works. The primary flow becomes entrained in the secondary flow. The Coanda effect causes the secondary flow to wrap along the curved surface of the CSM. The result is a vectoring of the primary flow or the flame spray.

CHAPTER 2

LITERATURE REVIEW

A great deal of research has been conducted on thermal spray with the main objective being to prove a particular gun technology, a particular spray method and/or a particular powder. In the case of this study, attention will be focused on proving a new gun technology: the CSM collar. Particular attention will be payed to the quality and efficiency of the sprayed NiAl deposit while using the CSM. Although it is expected that vectored spray depositions will resemble normal spray depositions, an extensive review of off normal spray studies has been performed as a reference for comparison. This section will present and discuss the discovered characteristics of several off normal thermal sprays studies. It has been broken into two main chapters: Splat Formation Characteristics and Deposit Characteristics. The first chapter will focus on the micro scale characteristics of single splats while the latter chapter will focus on the macro characteristics of the sprayed deposits. Within each chapter are sections and within each section are descriptions of what specific researchers have found about a particular deposit characteristic. This method has been used to provide easy reference to a particular study for a particular deposit characteristic.

Splat Formation Characteristics

Coatings are created by the continual addition of individual molten splats. The properties of these individual splats can be influenced by the spray angle parameter as well by gun parameters, surface parameters and atmospheric parameters. In this study the influence of changing the spray angle parameter will be considered. The main

characteristics of individual splats that are influenced by the spray angle are the effective diameter, circularity and splashing. Variances in these characteristics are often associated with changes in the coating characteristics. For instance the degree of splashing can influence the coating surface roughness. Most off-normal splat formation research has been performed to aid in the development of numerical spray simulations to optimize robotic mapping. The following sections will discuss some of the research and results that have been published.

Effective Diameter

When particles are sprayed they are usually nearly spherical as they fly through the atmosphere. However, when they impact onto the substrate surface they almost never impact as a perfect circle. One way of physically describing these splats is by their Equivalent Diameter:

$$ED = \sqrt{\frac{4A}{\pi}} \tag{1}$$

where *A* is the splat area. Montavon et al. [5] found through optical observation and Gaussian analysis that the *ED* of vacuum plasma sprayed (VPS) Astroloy particles does not change as the spray angle changes.

Circularity

Due to the momentum of the sprayed particle and the relative angle of the substrate to the axis of the gun the circularity of the splat may deform into a more elliptical shape. One physical description of this is the Elongation Factor:

$$EF = \frac{\pi L^2}{4A} \tag{2}$$

where *L* is the longest dimension across the splat. Montavon et al. [5] found in the same way for *ED* that *EF* does change as spray angle changes.

Based upon Madejski's [6] results Kanouff et al. [7] defined the fraction of splat material upstream from the impact point as:

$$f = \frac{\theta}{180^\circ} \tag{3}$$

Kanouff et al. [7] developed *f* for a numerical model using the string method to predict surface roughness. The results over predicted the coating thickness, but accurately portrayed the amount of roughness.

Kang and Ng [8] through optical SEM observations concluded that the impact point of the particle could be found through a backtracking method as accurately as employing a geometric formula. Through the backtracking method they traced back several of the finger-like protrusions of the splats (Figure 6). Where these lines intersected was the impact location. However, tracing these lines back to their intersection point was noticeably tedious and time consuming. The geometric formula method found the impact location by calculating the foci locations of the splat's elliptical shape. Upon comparing the two methods they found them to be within about 7% of each other. Both of these methods showed that the distance between the impact point and the center of the ellipse increased as the spray angle decreased.

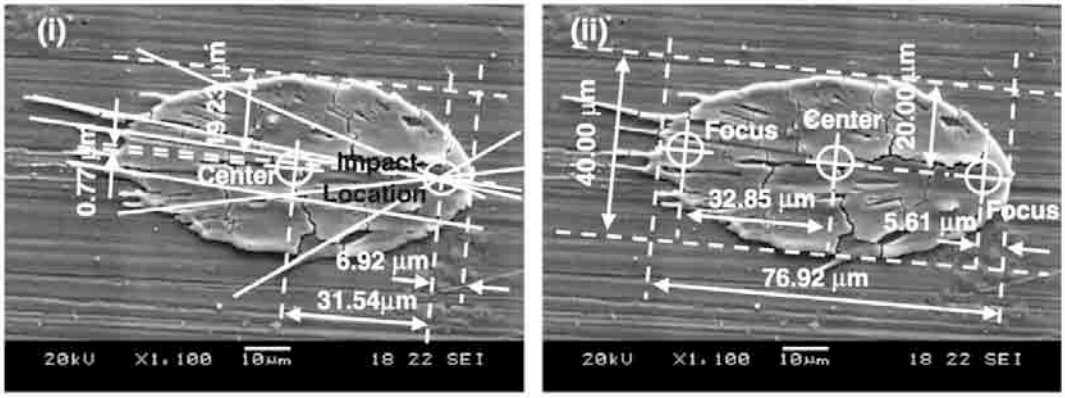

Figure 6 A splat impact schematic. The impact points in these splats can be traced back by backtracking the finger like protrusions to a focal point. Alternatively the location of the impact location can be found mathematically by calculating the foci locations [8].

Bussman et al. [9] found by using a 3D numerical model that more than 90% of the particle's material spreads downstream from the point of impact for spray angles less than 45°.

Splashing

As the particles impact the surface they splash sending finger like protrusions outward from the point of impact. Montavon et al. [5] described the degree of splashing by the following equation:

— (4)

where *P* is the perimeter of the splat formation. They found that the *DS* does not change much based upon spray angle in the same manner as they did for measuring the *ED* and *EF*. Kang et al. [8] through optical SEM observation found that the splashing becomes more unidirectional due to the particle's momentum as the spray angle decreased as shown in Figure 7 (a)-(g) where Figure [fig:Individual-splat-formations] (a) is the splat

formation of a perpendicularly sprayed particle and (b)-(g) are splats formations sprayed at off-normal angles. Smith et al. [10] through optical observation found that the degree of splashing increased dramatically as substrate surfaces became rougher (Figure 8)

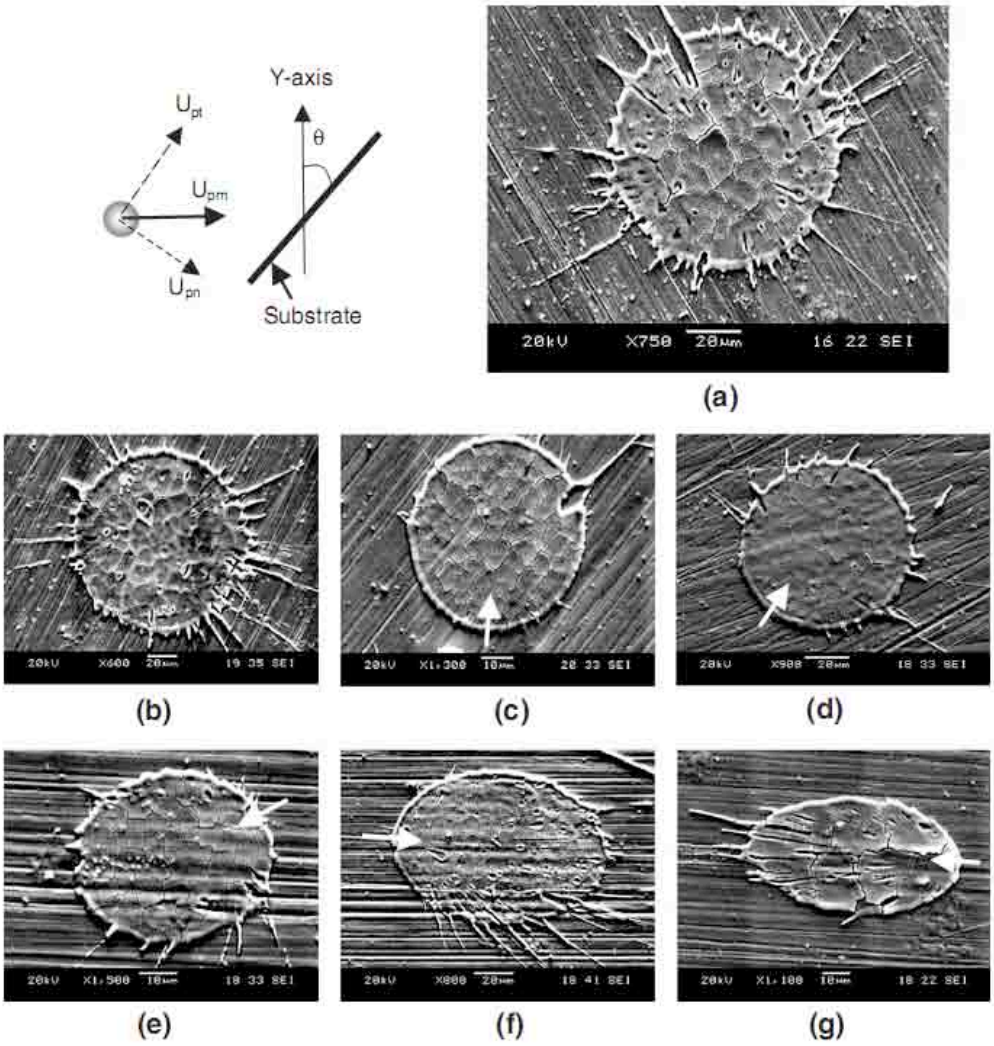

Figure 7 Individual splat formations sprayed at various angles. Figures (a)-(g) show the change in splat formation as the spray angle decreases from 90º. The fingerlike protrusions become more unidirectional as the spray angle decreases and the splats themselves become more elliptical [8].

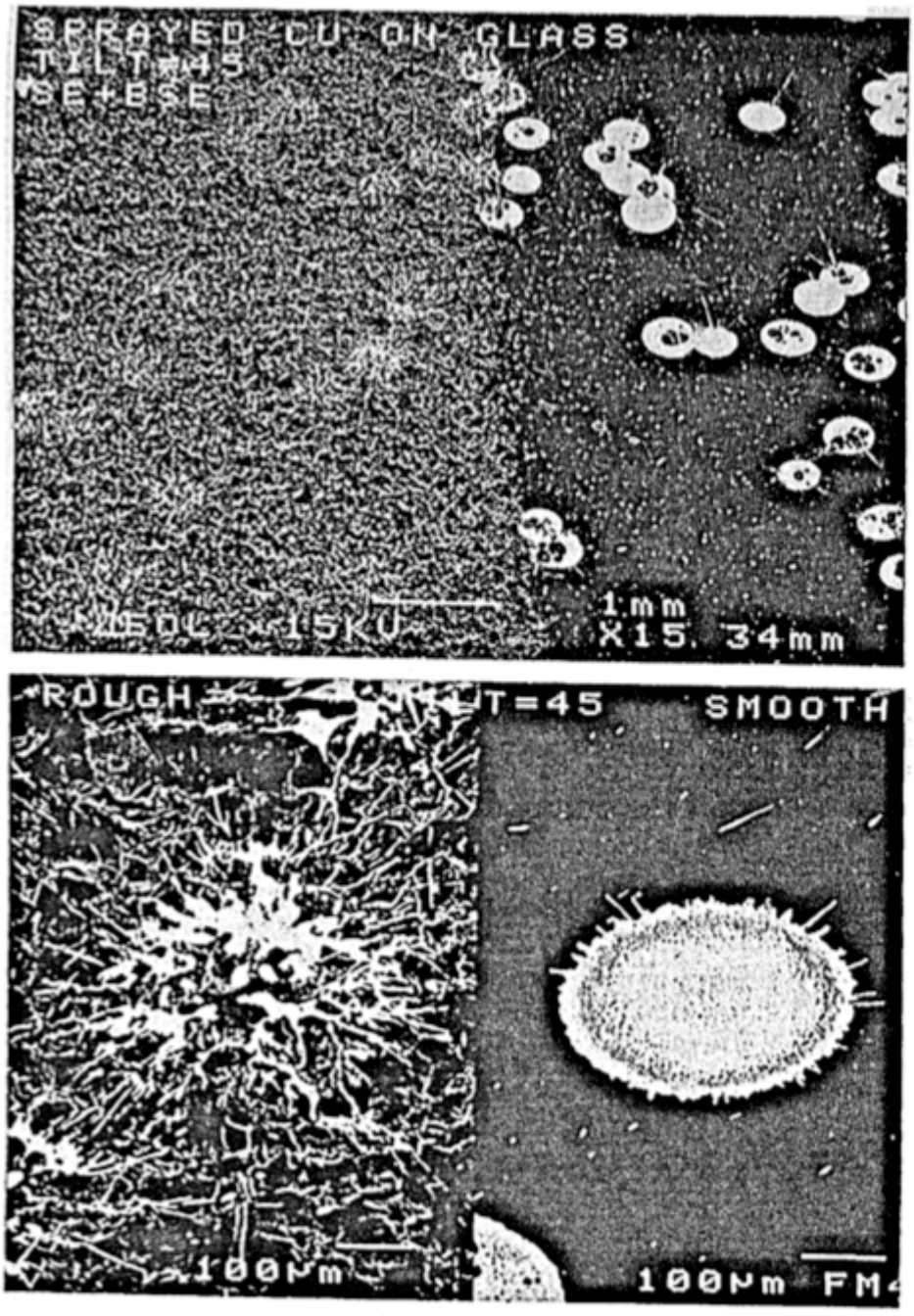

Figure 8 Surface roughness influence on splashing. These two images show the effect of surface roughness on the degree of splat splashing. The bottom image is zoomed to show the distinct differences in splat formation. The image on the bottom left is a splat formation on a rough substrate whereas the image on the bottom right is a splat formation on a smooth surface. The degree of splashing increases when the substrate surface roughness increases [10].

Deposit Characteristics

As splats begin to build, a coating begins to form. These coatings tend to range from a few micrometers in thickness to a few millimeters. The coatings have important "macro" properties that can be different than the properties of the individual splats and the properties of the original bulk material. These "macro" properties are what primarily characterize the deposit. The following sections present and discuss common material properties that have been researched in off-angle spray studies.

Porosity

Tiny pores in the coating begin to form when splats do not completely form to the substrate. It is usually desirable to minimize the number of pores in the deposit because the presence of pores is associated with a decrease in density, an increase in surface roughness Smith et al. [10], a decrease in surface hardness and a decrease in tensile strength [8,11]. When spray angles are decreased, a resultant increase in porosity percentage occurs. Studies performed by Montavon et al. [5], Smith et al Smith et al. [10], Ilavsky et al. [12], Leigh and Berndt [11] and Tillmann et al. [3] have all shown that the percentage of porosity increases as the spray angle decreases. By contrast, a few recent studies by Strock et al. [13] and Houdkova et al. [14], have reported results that demonstrated porosity did not change significantly as the spray angle diminished. The key difference between these two different results was the velocity of the sprayed particles with the former studies using Plasma Spray guns and the latter studies using HVOF spray guns. The findings by these studies are shown in Figure 9 and Figure 10.

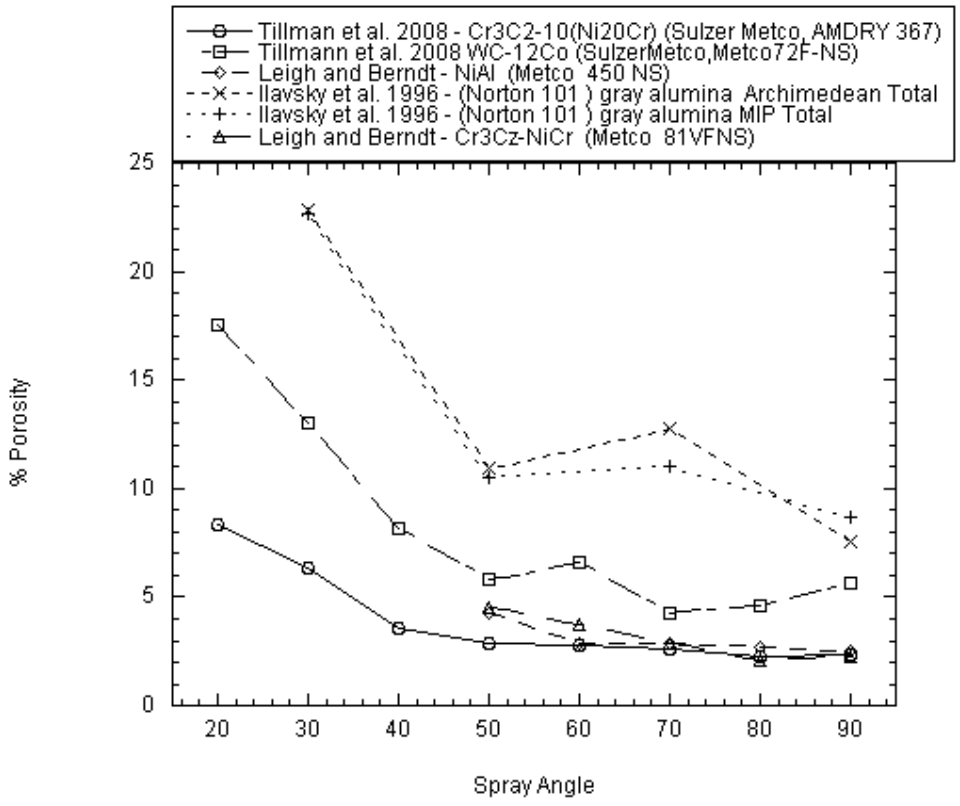

Figure 9 Porosity data plots [3,11,12].

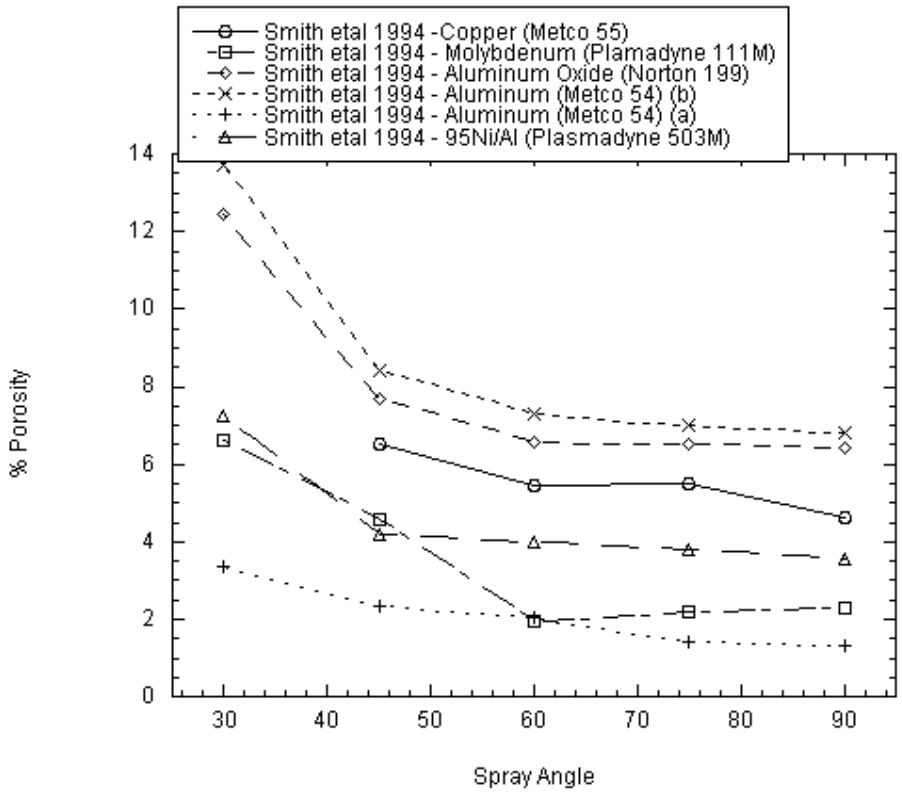

Figure 10 Porosity data plots (Continued) [10].

The momentum of a sprayed particle is critical to how well a particle will form to the sublayer. When a particle is sprayed perpendicular to the surface of the substrate all of that particle's momentum contributes to the impacting and spreading of the particle across the sublayer forming a splat. When the normal momentum is sufficient the splat can fill in the tiny cracks and crevices of the sublayer. Most thermal spray guns spray in a cone shape, so inevitably some of the particles sprayed will be sprayed off-normal. Thus those particles will have a lower normal momentum Figure 11.

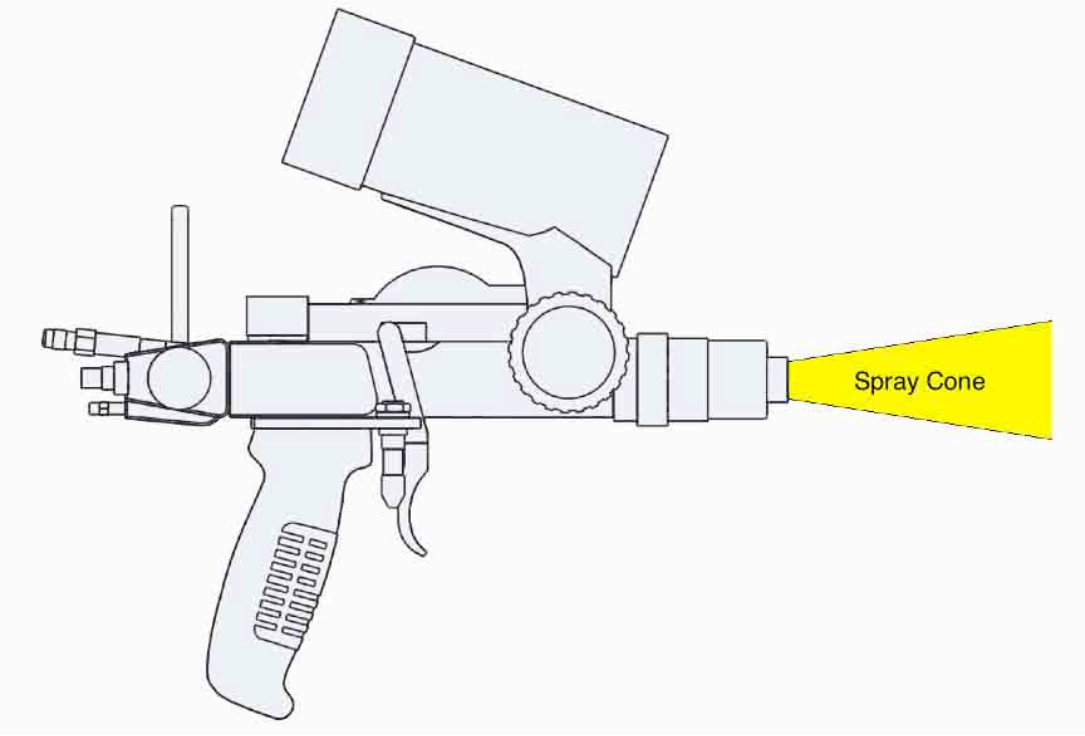

Figure 11 A typical thermal spray cone zshematic. A typical spray cone shape of a thermal spray gun.

When the spray angle begins to decrease, the momentum of the particle begins to be spread between two directions, the *x* and the *y*, where *x* is parallel to the surface of the substrate and y is perpendicular to the substrate. The momentum in the two directions are defined as P_x and P_y Figure 12. When the particle is sprayed perpendicular to the surface, $P_x=0$, a relatively symmetric splat forms. As the spray angle decreases the magnitude of P_x begins to increase and the magnitude of P_y decreases. When the magnitude of P_x increases, the momentum of the particle causes the splat to spread. This has a tendency to thin the splat formation and inhibit the filling of sublayer pores and cracks.

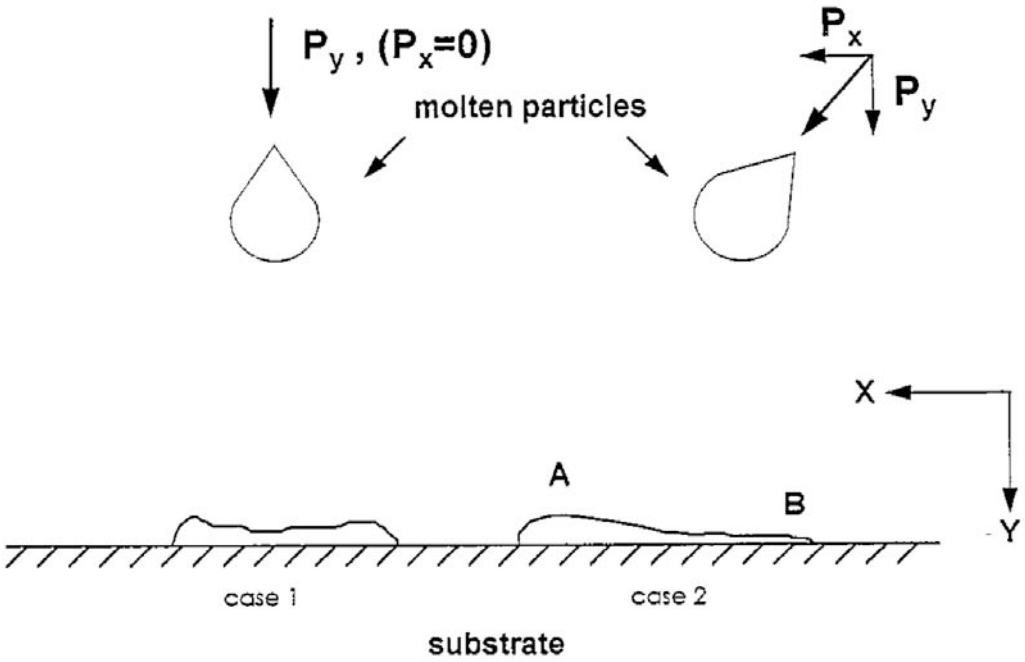

Figure 12 Momentum in splat formations. This figure showcases the change in directional momentum between the perpendicular and off-normal cases. As the spray angle decreases more momentum begins to transfer to the transverse x-direction. This increase in the P_{x} causes the splat formations to become uneven as shown in case 2 in this figure [11].

In addition, as the spray angle is decreased another major obstacle to limiting pore formation appears: the shadow effect. The shadow effect can easily be seen in Figure 13. It occurs as rough peak like features begin to form. These peaks work to block incoming particles from the backside of their surfaces. The shaded areas of these peaks soon become voids as more and more particles are sprayed [10,11].

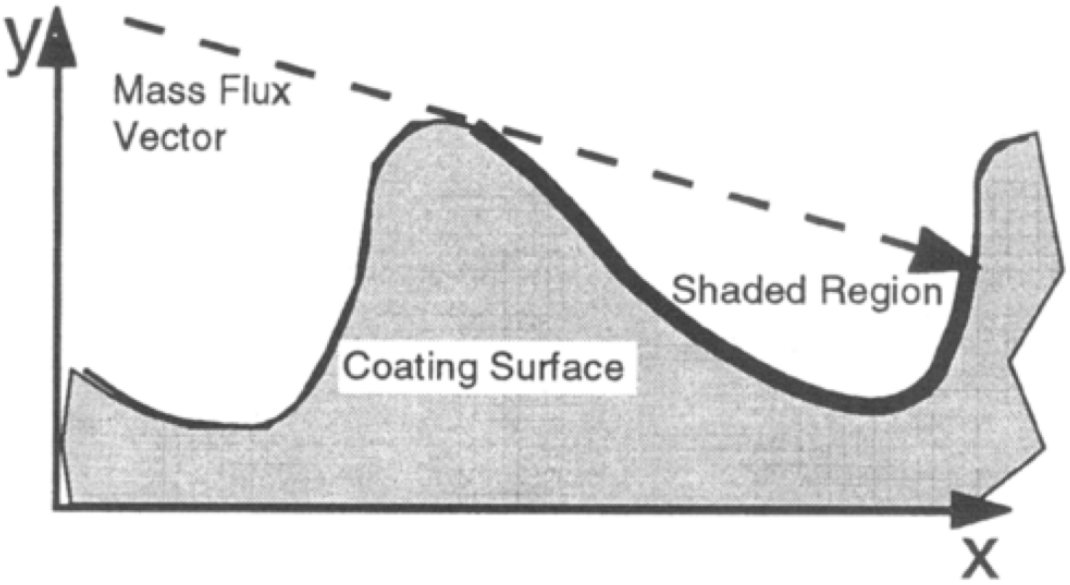

Figure 13 The shadow effect. The shaded region is a result of the shadow effect caused by the decreased spray angle. The shaded region becomes a potential void when off-normal splats follow the dashed line trajectory. These voids result in increased porosity levels [7].

As these coatings continue to build up they begin to take on characteristics associated with the spray angle. Smith et al. [10] found through optical observations that when molybdenum powders were sprayed at certain angles that column like formations in the deposit would build up at about the same angle as the spray angle (Figure 14). Similarly, Ilavsky et al. [12] found through optical observations of yttria-stabilized-zirconia deposits that two types of pores formed: interlamellar pores and intralamellar cracks. The interlamellar pores were mostly oriented parallel to the substrate and did not change with spray angle. However, the intralamellar cracks did change and were oriented towards the spray direction. This study suggested that this was due to the preferred crystallographic orientation of the grains within the splats. This was likely caused by the cooling direction associated with the spray orientation (Figure 15).

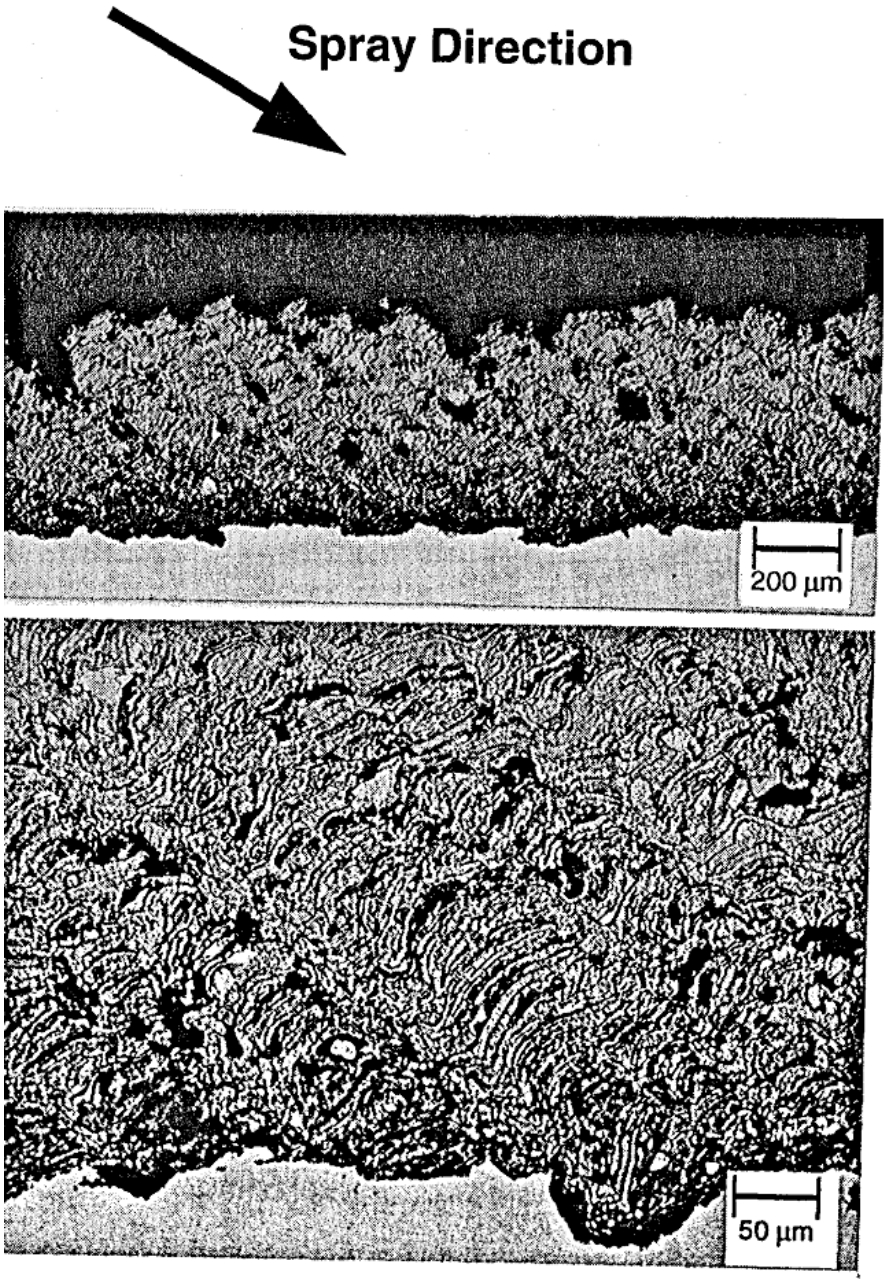

Figure 14 Polished and etched molybdenum sprayed at 30 degrees. This figure shows the tendency of the splats to form in a direction in correlation to the particle spray angle. This is a likely result of the preferred crystallographic orientation [10].

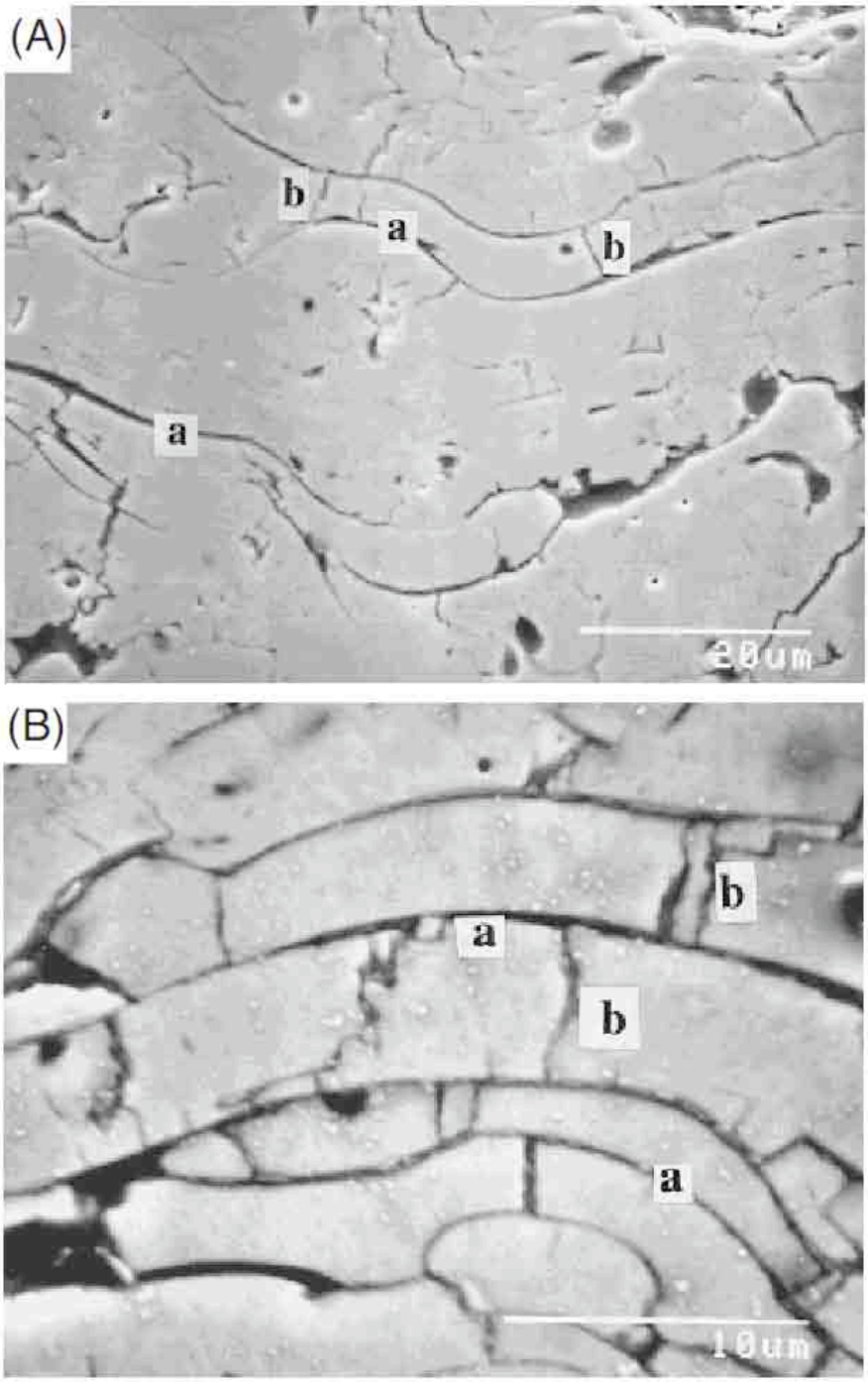

Figure 15 Typical microstructure of plasma sprayed ceramic deposits. These micrographs show the two types of cracks found in an yttria-stabilized-zirconia deposit. a) interlamellar pores and b)intralamellar cracks [12].

Dramatic increases in porosity as well as most of the other deposit properties start to occur when the spray angle reaches the 45° mark [3]. At the 45° mark the magnitude of P_x equals the magnitude of P_y and any decrease in the spray angle causes $P_x > P_y$. At this point more of the particle's energy is spent moving the particle downstream on the surface than into the surface. Theoretically, when the spray angle reaches 0 the particles will never impact onto the surface. Note: Strock et al. [13] and Houdkova et al. [14] did not report any of their porosity measurements in their HVOF studies.

Surface Roughness

In some applications, such as the coating of cylinder bores, it is desirable to minimize the surface roughness of the deposit in order to reduce post-processing costs [7]. Studies by Kanouff et al. [7], Leigh and Berndt [11], Smith et al. [10] and Tillmann et al. [3] have all found that the surface roughness of sprayed deposits increase as the spray angle decreases. Other parameters that affect surface roughness include initial particle momentum, substrate roughness and particle size.

Effect of Particle Momentum on Surface Roughness

When a splat hits a surface it begins to spread out. The direction of this spreading is dependent on the direction of its momentum relative to the surface (Figure 12). As discussed above the momentum parallel to the substrate surface begins to increase as the spray angle decreases. This increase in the parallel momentum aids in the spreading of the splats causing the splats to shoot out smaller particles downstream called “overspray” (Figure 16). The overspray particles re-impact onto the surface at angles much less than the original spray angle and usually adhere to the higher asperities downstream. This

action increases the surface roughness of the deposit [7,10]. If the downstream surface roughness is already high then the spray angle and surface roughness tend to work together to increase surface roughness.

Kanouff et al. [7] conducted a surface roughness study using a plasma torch spraying an unspecified powder. Figure 17 shows the measured surface profile of the deposit they formed by spraying several passes in the direction perpendicular to the x-y plane at an angle of 51°. The large hump shape, located in the impact zone of Figure 17, was actually delamination of the deposit due to residual stresses and buckling, but it can be seen that zones 3-5 have much higher relative surface roughness due to the overspray adhering to the asperities when compared to zones 1 and 2. Through trial and error they measured and confirmed that oversprays impacted at lower angles found in Table 1.

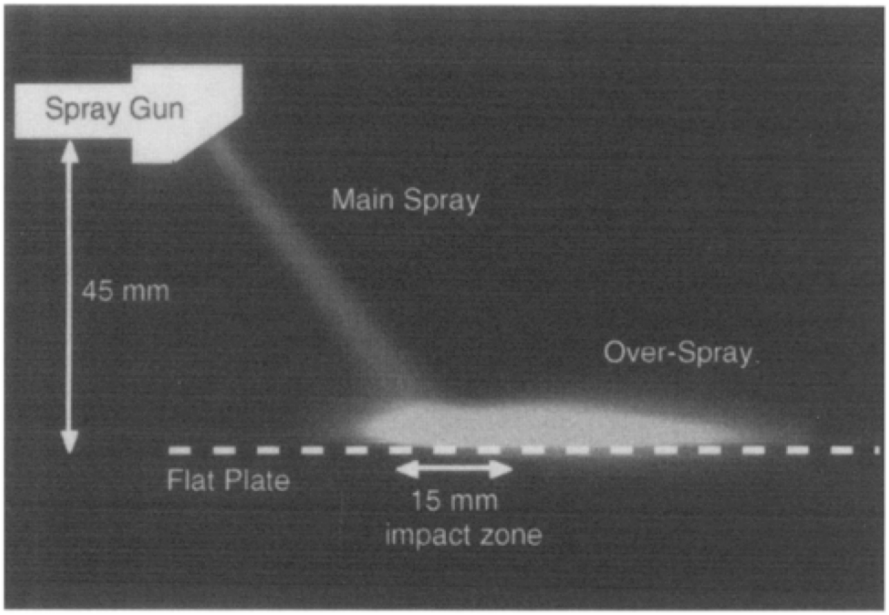

Figure 16 An image showing the over spray region. This image shows the over spray region indicated by the elliptical white zone parallel to the flat plate. It is most likely made up of smaller particles that have splashed away from the initially impacting particles [7].

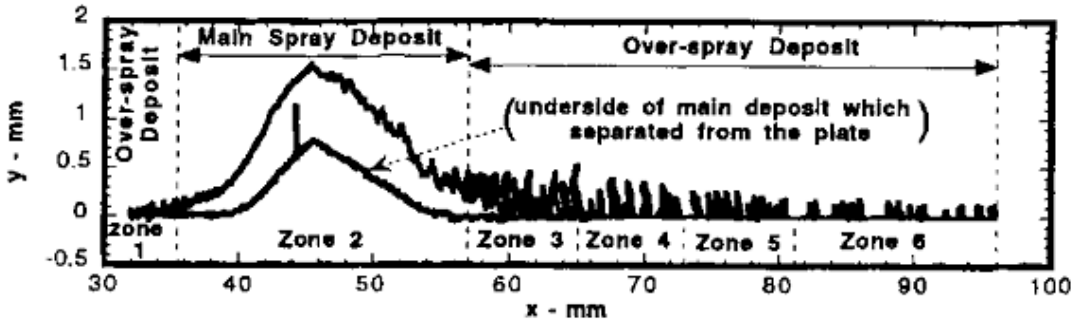

Figure 17 The surface roughness of the spray in reference to their zones. Zones 3-5 have much higher surface roughness in comparison to zone 2. This is likely due to the overspray splashing and the particles adhering to surface asperities [7].

Table 1 Distributions For the Deposited Mass, Direction Angle, and Droplet Size [7].

Zone No.	Description	Thermal spray direction angle (θ), degrees	Droplet size (D), µm	Deposited mass (w), %
1	Overspray	178	5	1
2	Mainspray	51	40	76.6
3	Overspray	7.5	15	14.4
4	Overspray	5	15	4
5	Overspray	3	10	2
6	Overspray	2	5	2

Houdkova et al. [14], Strock et al. [13] and Bach et al. [15] all performed off-normal thermal spray studies using HVOF guns which spray materials at supersonic velocities. They all actually found that the surface roughness of the coatings went down as the spray angle decreased. They suggested that at lower angles the impacting particles were becoming more elongated instead of spiked and were likely breaking off asperities thus making the surfaces smoother. However, for lower velocity processes, the surface roughness usually increases as the spray angle decreases. The findings for the surface roughness for all of the studies discussed are shown in Figure 18-Figure 20.

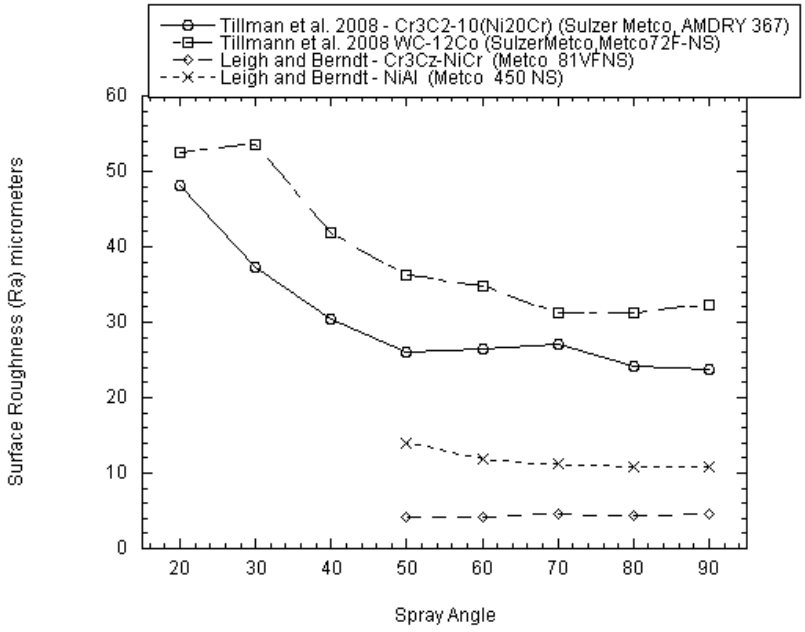

Figure 18 Surface roughness data plots[3,11].

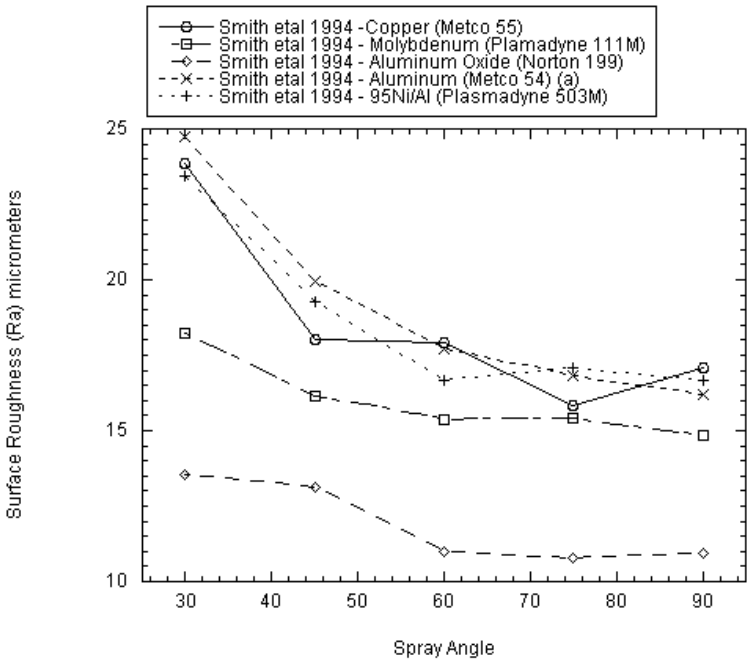

Figure 19 Surface roughness data plots (continued)[10].

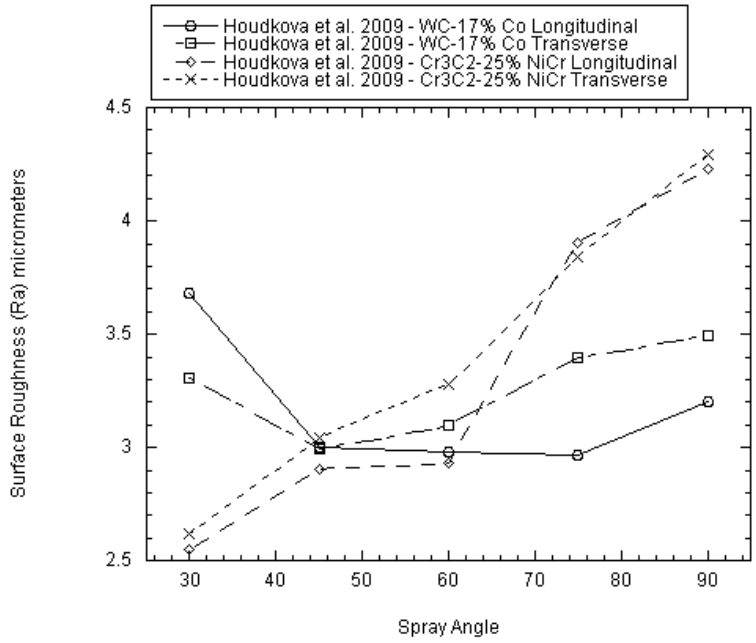

Figure 20 Surface roughness data plots (continued) [14].

Effect of Particle Size on Surface Roughness

If the powder size is sufficiently small then the spray angle tends to have little effect. Essentially, what happens is the smaller size of particle is better suited for filling in the cracks and crevices of the substrate. Leigh and Berndt [11] and Smith et al. [10] conducted studies using different plasma sprayed powders each with different average diameters (Table 2). They both found that for the smaller sized powders the overall roughness tended to be less than the larger powders. In the study by Leigh and Berndt [11] it was the Cr_{3}C_{2}-NiCr powder and in the study by Smith et al. [10] it was the Aluminum Oxide powder that showed the least amount of surface roughness. Their specific findings for the surface roughness of small diameter powders can be found in Figure 21 & Figure 22.

Table 2 Powder Diameters

Powder	Average Powder
Cr_3C_2-NiCr [11]	24.6 µm
NiAl [11]	58.4 µm
Aluminum [10]	≈80 µm
Copper [10]	≈70 µm
95 Ni/5 Al [10]	≈80 µm
Molybdenum [10]	≈70 µm
Aluminum Oxide [10]	≈50 µm

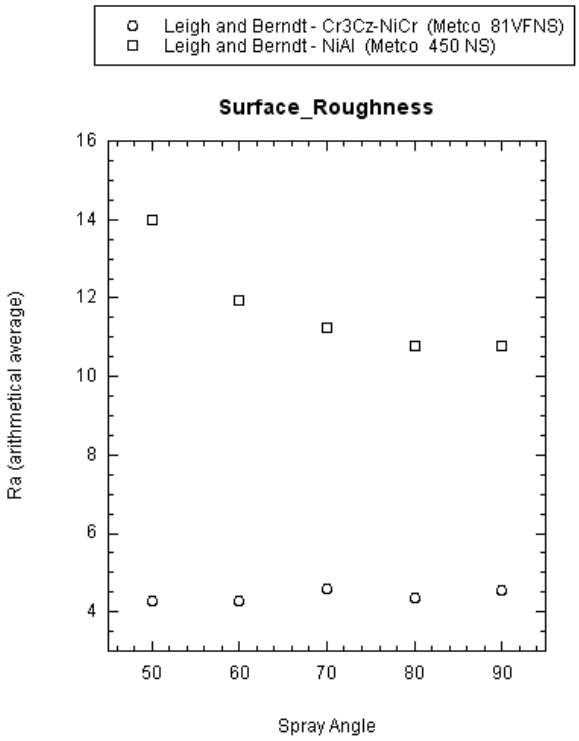

Figure 21 Surface roughness of small diameter powders [11].

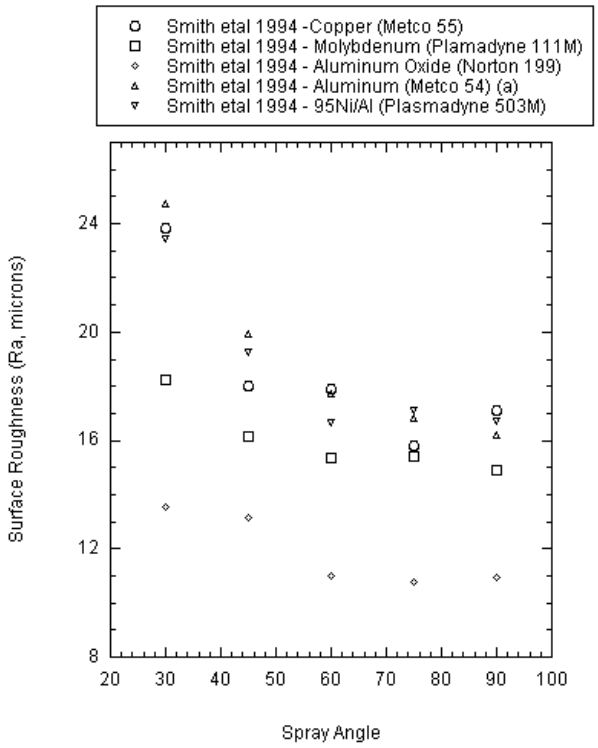

Figure 22 Surface roughness of small diameter powders (continued) [10].

Hardness

The hardness of sprayed coatings can be quite different than the hardness of the original bulk material or even the hardness of individual splats due to the inclusion of pores within the coatings. It is no surprise that the hardness of coatings tends to decrease because pores tend to be more prevalent as spray angles decrease. Leigh and Berndt [11], Strock et al. [13] and Houdkova et al. [14] all reported decreases in microhardness of the materials that they tested, using the Vickers Hardness Test method, as the spray angles decreased. Houdkova et al. [14] also reported a decrease in hardness using the HR15N method. Interestingly, these studies combined used HVOF and plasma spray guns showing that the hardness decrease was not dependent on either spray process. However, Montavon et al. [5] and Tillmann et al. [3] (both using the Vickers Hardens Test Method)

found that their hardness results showed no conclusive correlation to the spray angle. Montavon et al. [5] concluded that the variations measured were due to the heterogeneous nature of the material. The findings of each hardness study are shown in Figure 23 & Figure 24.

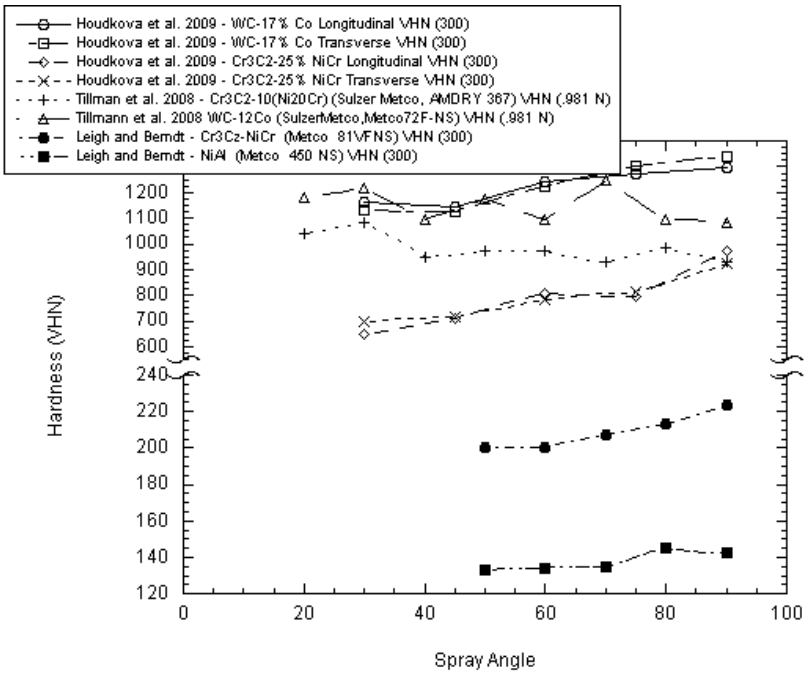

Figure 23 Measured coating hardness [3,11,14].

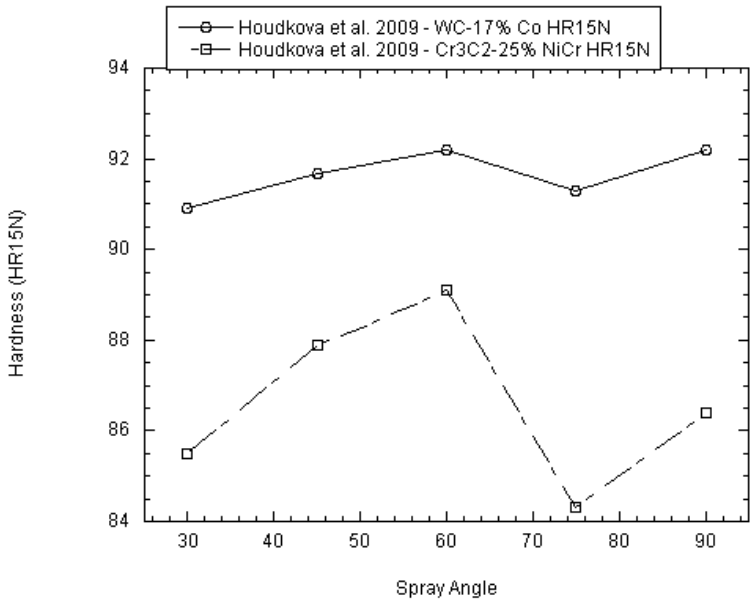

Figure 24 Measured coating hardness [14].

Tensile Strength

The tensile strength, σ, is represented by: $\sigma = \frac{F}{A}$, where F is the maximum axially applied force and A is the cross sectional area perpendicular to the applied force. Any given material has an ultimate tensile strength, σ_{ult}, at which that material carries the maximum load. Coatings tend to have more voids within a cross section than a cross section of the same material in cast form. These voids decrease the overall cross sectional area and in turn decrease the effective tensile strength. From the previous section it is known that the overall porosity for sprayed coatings increases as the spray angle decreases, which in turn affects the tensile strength. Leigh and Berndt [11], using the ASTM C 633 testing method, and Tillmann et al. [3], using the DIN EN582 testing method, both found this to be the case in their studies. Their findings are shown in Figure 25.

Kang and Ng [8] noticed that individual splats had a greater tendency to show peeling at lower spray angles under the microscope Figure 26. They believed that the poor adhesion was due to a reduction in the normal momentum of the particle. Leigh and Berndt [11] made similar conclusions stating that interlamellar bonding decreased as the spray angle decreased.

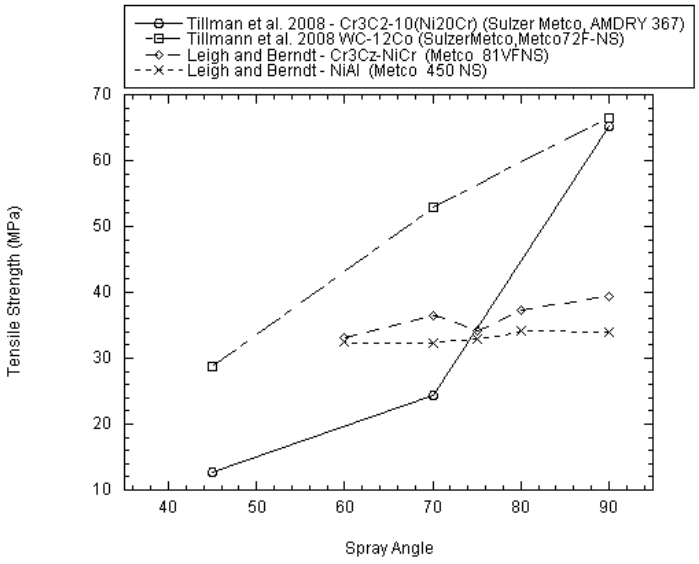

Figure 25 Measured coating tensile strength [3,11].

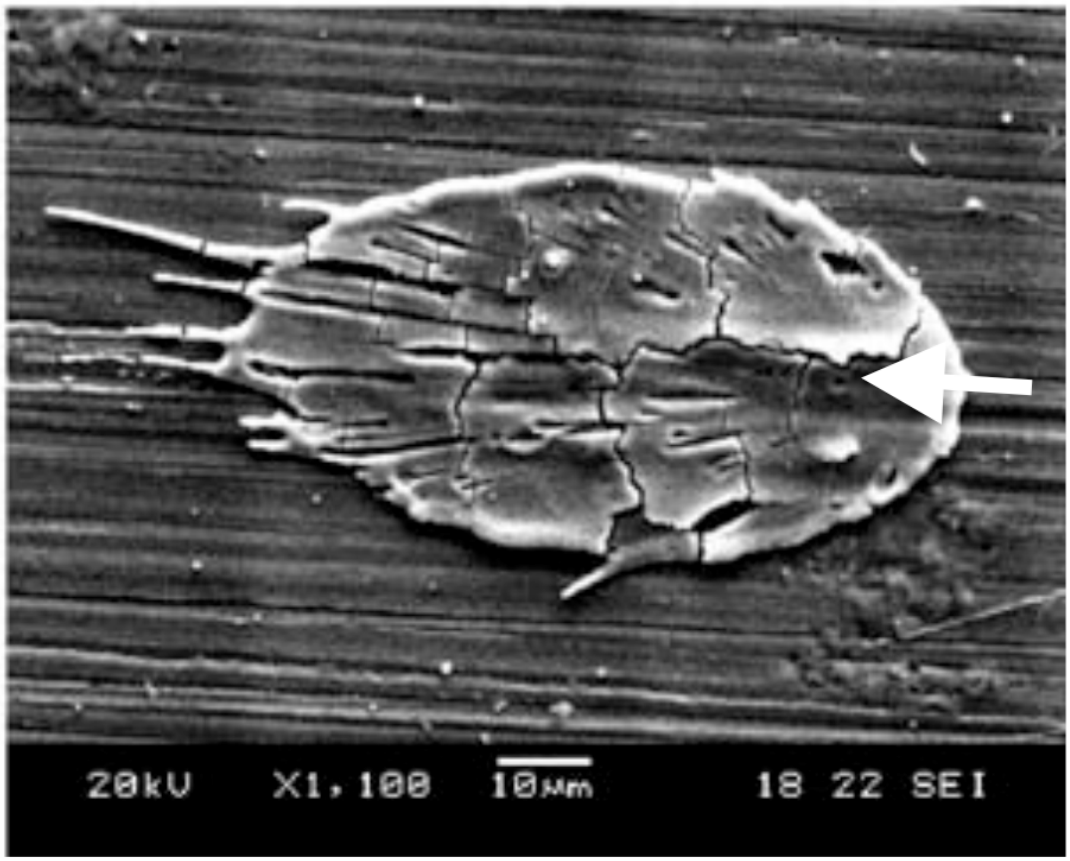

Figure 26 Spalling due to a decrease in normal momentum [8].

CHAPTER 3

OBJECTIVES

Statement of Problem

The problem of this project is to determine basic materials properties of off angle thermally sprayed NiAl coatings using a novel spray manipulation nozzle attachment called the Coanda-Assisted Spray Manipulation. This project will focus on measuring the porosity, surface roughness, microhardness, and tensile strength of the sprayed material. Coatings will be sprayed using a Metco 5P II Thermal Spray gun, which is a combustion flame thermal spray gun, with and without a CSM collar. The measurable properties will be compared for un-vectored and vectored coatings. The project will determine if and how much the spray is affected by the CSM and vectoring the direction of the spray.

It is already understood that the optimal impingement angle of thermal sprays is 90º for most, if not all applications. Therefore, the coupon surface will be situated perpendicular to the spray angle of the CSM for testing purposes.

Statement of Purpose

1. To compare the properties of vectored and un-vectored thermally sprayed deposits of NiAl powder.
2. To provide substantial evidence for or against the use of the CSM collar.

Statement of Need

Thermal spray is used in a variety of industries such as aerospace, automotive, nuclear and more. Each industry uses it for a variety of barrier applications such as corrosion resistance, ablative material, thermal resistance, electromagnetic resistance and more.

Thermal spray applications are costly, inefficient and/or impossible because the spray cannot be applied due to surface orientation constraints. The CSM can help to minimize the thermal spray cost by increasing efficiency and cutting operation time therefore its effectiveness needs to be proven.

CHAPTER 4

METHODOLOGY

Statement of Conditions

1. Test will be conducted at room temperature in open atmosphere.
2. Temperature of substrate surface will be the same for spray in the un-vectored process as it was in the vectored process.
3. Exit flow velocity of primary and secondary gases will remain constant.

Statement of Limitations

1. The test will be conducted with only a Metco 5P Type II flame spray gun.
2. The test will be conducted with only one powder: NiAl.

Statement of Hypothesis

The goal of the test is to compare the spray material properties of vectored and un-vectored Nickel Aluminum powder. The properties of the vectored deposits will show results comparable to un-vectored deposits.

Setup and Preliminary Calculations

Each 2.54 cm diameter x 3.81 cm long 1018 steel coupon was placed in an ultrasonic bath with mild dish soap to wash off grease for 12 minutes and finally post wiped with ethyl alcohol to remove any remaining water before processing. Three sample coatings of Metco 450NS (NiAl) powder were created using a Metco 5P II gun for each test as shown in Table 4 where the coupons are identified by the numbers 001-072. The

coupons for the vectored and un-vectored processes were positioned as shown in Figure 27 at impingement angles of 90° (perpendicular), 75°, 60° and 45° to the respective spray angle shown in Figure 28. Figure 29 indicates the movement path of the spray gun for both processes. The gases used were oxygen and acetylene, which were set at the same flow rate of 35 CFH as indicated in Table 4. Filtered, compressed air set between 4-5 CFM was used as the gas for the secondary flow.

Table 3 Flame Spray Parameters

Parameter	Type	Flow Rate	Composition
Primary Flow Gas	Oxy/Acetelyne	Oxygen-35CFH / Acetelyne-35 CFH	-
Secondary Flow Gas	Compressed Air	4-5 CFM	-
Powder	Metco 450NS Powder (NiAl)	-	Al-4.99 (wt %), Ni-93.41 (wt %), T.A.O-0.3 (wt%), Org Solids-1.18 (wt%), Moisture-0.12 (wt%)

Each coupon was preheated at the #4 position for three cycles as shown in the bottom left corner of Figure 27. A cycle was defined as one back and forth motion. Next, the coupons were sprayed for a half cycle at each incremental height starting at the #1 position and ending at the #7 position followed by a post heating cycle at the #4 position. The deposition process was repeated 6 times for all coupons except for the tensile test coupons. Coupon samples 004-006, 010-012, 016-018 and 022-024 had an additional 6 passes sprayed in order to provide a thickness comparison. All of the finished coupons were left to air cool at room temperature.

Table 4 Test Design Matrix

Testing Procedure Matrix							
Spray Process	**Spray Angle (deg)**	**Porosity Measurement**	**Surface Roughness Measurement**	**Profile Measurement**	**Micro-hardness Measurement**	**Tensile Test T1 Thickness**	**Tensile Test T2 Thickness**
Vectored	**90**	049 050 051	049 050 051	049 050 051	049 050 051	001 002 003	004 005 006
Un-Vectored	**90**	061 062 063	061 062 063	061 062 063	061 062 063	025 026 027	028 029 030
Vectored	**75**	052 053 054	052 053 054	052 053 054	052 053 054	007 008 009	010 011 012
Un-Vectored	**75**	064 065 066	064 065 066	064 065 066	064 065 066	031 032 033	034 035 036
Vectored	**60**	055 056 057	055 056 057	055 056 057	055 056 057	013 014 015	016 017 018
Un-Vectored	**60**	067 068 069	067 068 069	067 068 069	067 068 069	037 038 039	040 041 042
Vectored	**45**	058 059 060	058 059 060	058 059 060	058 059 060	019 020 021	022 023 024
Un-Vectored	**45**	070 071 072	070 071 072	070 071 072	070 071 072	043 044 045	046 047 048

Front View

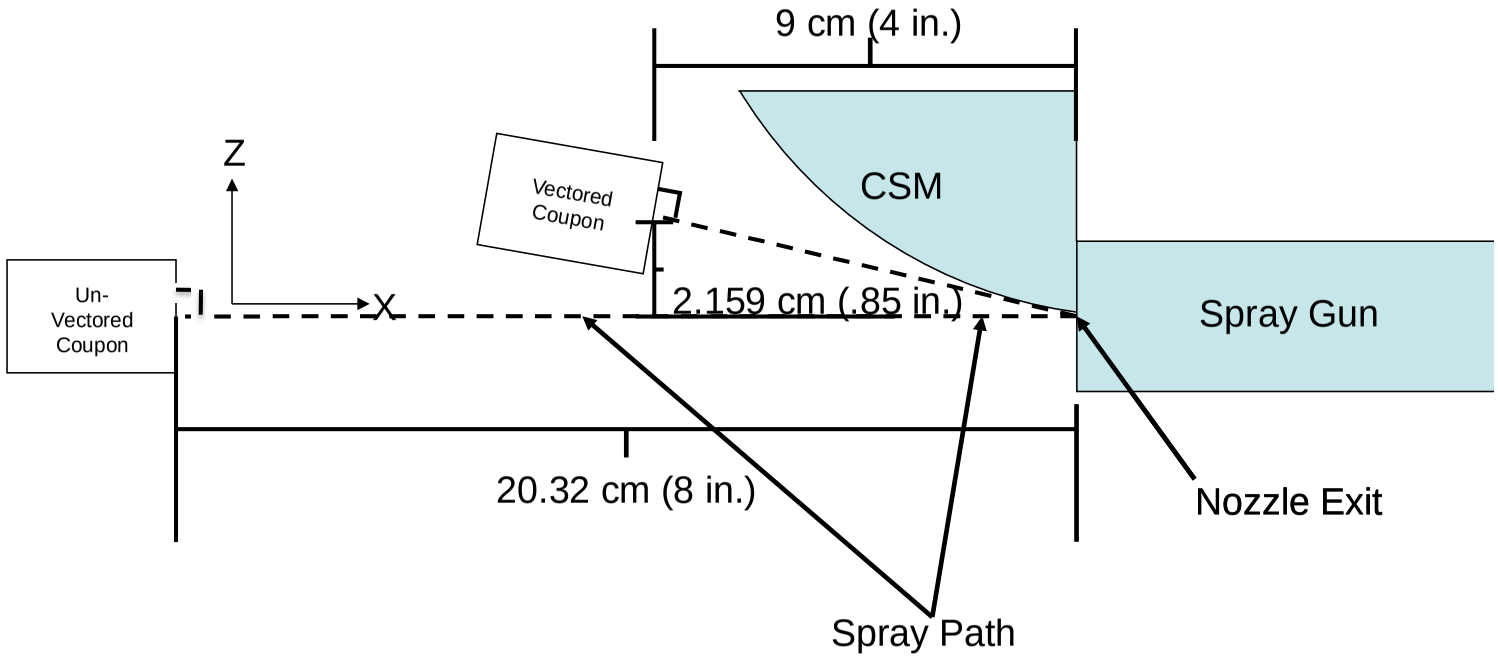

Figure 27 The front view of the coupon position schematic. This schematic shows the spray gun and coupon set up. The un-vectored coupons were positioned in line with the un-vectored spray 20.32 cm away. The vectored coupons were positioned in line with the spray 9 cm in the x-direction and 2.2 cm in the z-direction.

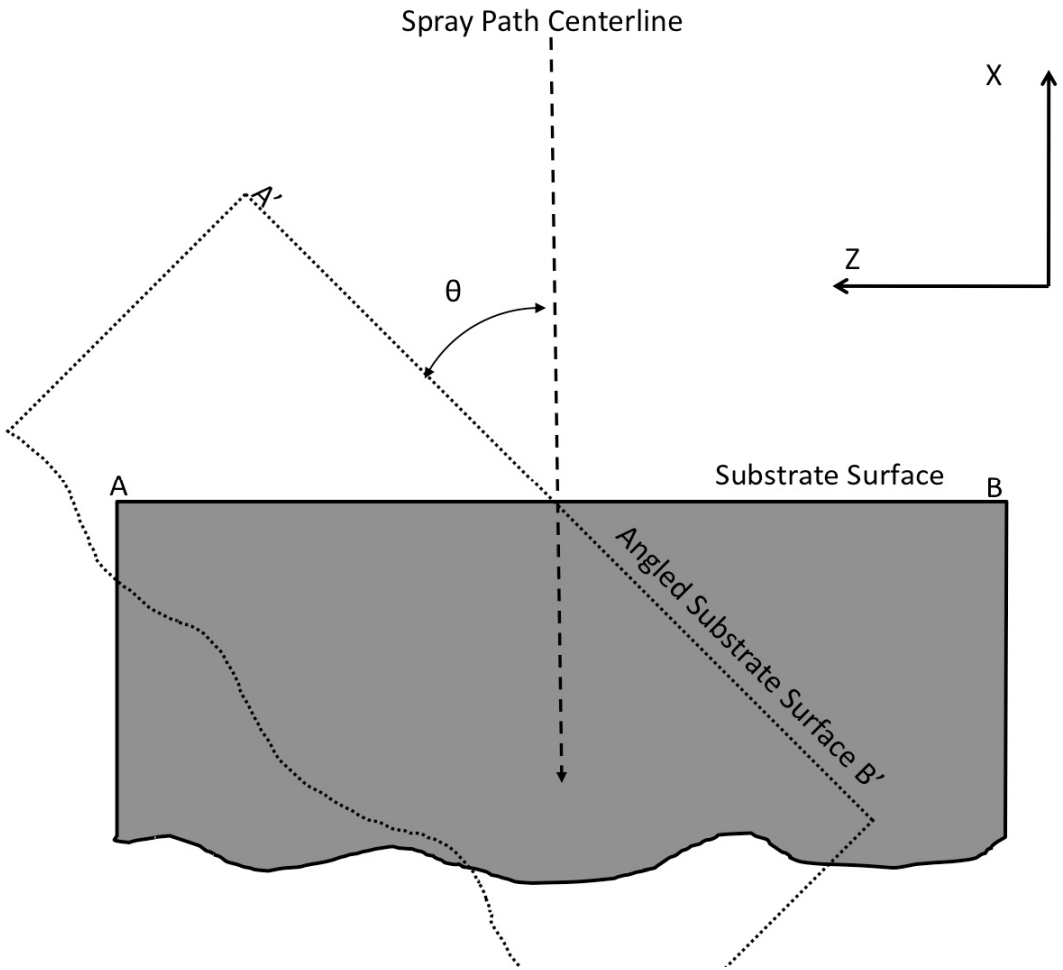

Figure 28 The coupon orientation schematic. This schematic shows the front view coupon orientation with respect to the spray path. θ varies from 90º - 45º for both processes.

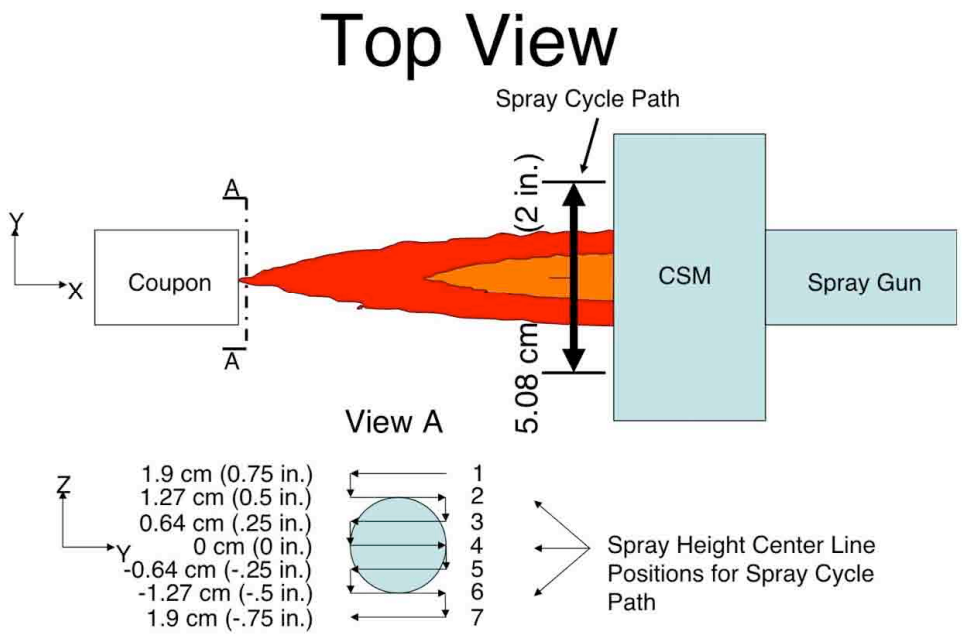

Figure 29 The cycle path schematic. This schematic indicates the spray path used to coat the surface of each coupon. A pre-heat cycle of three back and forth sweeps was performed at position height 4 followed by a spray cycle (View A) starting at height 1 and proceeding to height 7. This was followed by a post heating cycle of one back and forth sweep at position height 4 followed by then next spray cycle. Six spray cycles were performed for each sample except for the T2 samples for the tensile test which were done with 12 spray cycles.

Spray Angle Setup

No data was available concerning the parameters affecting the spray angle for the vectored flame spray process prior to this study. It was assumed that the spray angle was a function of primary flow rates, secondary flow rates, powder feed rate and CSM collar geometry. The spray angle was experimentally found by varying the secondary flow rate from 4 CFM to 9 CFM while keeping all other parameters constant. The method for measuring the spray angle consisted of taking 10 digital images of the vectored spray particles at an incremental secondary flow rate. The images were then analyzed using a "center of light intensity" method and geometric principles to measure the spray angle. The "center of light intensity" method was based off of a similar method one would use for calculating the center of mass. Two parallel columns of pixels were chosen from the image at a set width of 200 pixels apart far enough away from the nozzle exit to only show light from the molten particles. These columns were then truncated down to the rows that only represented the cross section of the sprayed particles while keeping the same row labels. Then the center of intensity, CI, was calculated for each column using Equation 5:

$$CI_1, CI_2 = \frac{\sum_{n=r_i}^{r_f} n \times I_n}{\sum_{n=r_i}^{r_f} I_n} \tag{5}$$

where r_i is the initial row number location, r_f is the final row number location and I_n is the intensity level at that particular row. This was repeated for both columns. The result was an estimated row location for the center of intensity. The number of rows between the

two centers of intensity was calculated and then used in Equation 6 to calculate the spray angle.

$$Spray\ Angle = \tan^{-1}\left(\frac{CI_1 - CI_2}{200}\right) \quad (6)$$

The two white lines in Figure 30 indicate the basic location of where the columns' pixels were chosen from the digital images. Table 4 lists the parameter settings for the spray angle measurements. The table indicates that the only parameter that was varied during the measurement was the flow rate of the secondary gas. The spray angle measurements are shown in Figure 31. Based upon the measurements indicated in Figure 31 the secondary gas flow rate was set between 4 and 5 CFM for an average spray angle of 9° which is an average of the angles measured at 4 and 5 CFM. The error bars represent the variance of the spray angle with 95% confidence level for ten samples.

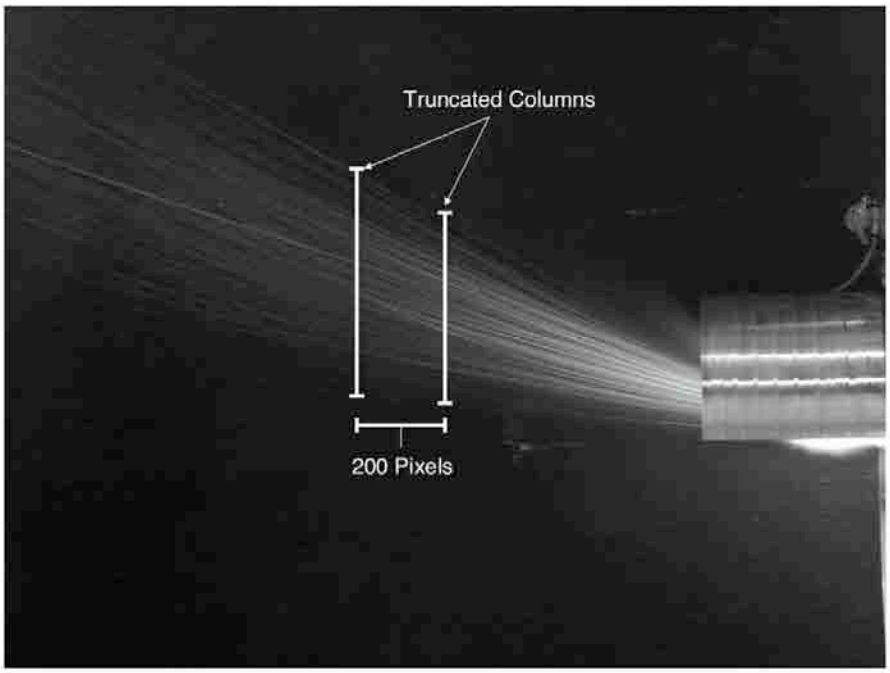

Figure 30 A digital image of the vectored spray and column truncation method. This image shows a typical vectored spray profile. The white lines indicate the column of pixels selected in order to determine the center of intensity which were in tum used to calculate the spray angle.

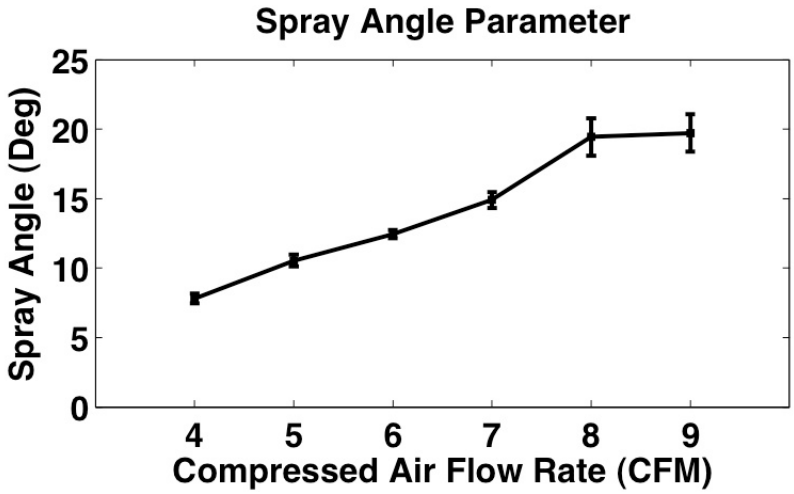

Figure 31 Plot of the measured spray angle vs. the volumetric flow rate of the secondary gas.

Constant Temperature Setup

An isothermal comparison was desired between the vectored and un-vectored spray process. In order to achieve this a type K thermal couple was mounted at the substrate surface to measure the peak temperature for an un-vectored coupon during the preheat cycle. Each measurement started at room temperature and was conducted 17 times. The average measured peak temperature was 339.1 C (642.4 F) with a 95% confidence error of ±6.6 C (±11.9 F). Next, the temperature was measured the same way along the vectored spray angle path until a similar temperature was measured. The location as indicated in Figure 27 measured an average temperature of 335.8 C (636.4 F) with a 85% confidence error of ±12.4 C (±22.4 F). Moving the coupon distance will have an effect upon the sprayed particles' impact kinetic energies and time dependent temperature distribution.

Time Dependent Temperature Profile and Impact Energy Calculations

In association with the microhardness and tensile strength measurements an estimation of the time dependent temperature profile and kinetic energy was performed for the Ni particles in the spray to understand the thermal and impact energy differences of the sprayed particles during the two different spray processes. This was done to help explain differences between the two processes for their material properties. These calculations were based upon the assumption that the particle's velocity in relation to the surrounding gases was very low (Re < 1) and that the heat transfer coefficient was very high (h = 10,000 W/m^{2}K) due to the presence of phase change. Table 5 shows the parameters used for these calculations which were based upon the previously mentioned assumptions, reported material properties, and test setup. The results from these

calculations do not represent accurate energies and temperatures because of the arbitrary parameters used. However, the estimated differences between the energies and temperatures for the two processes were useful for explaining the different material properties between the two.

Table 5 Assumed Parameters Used to Calculate the Time Dependent Temperature Profile.

Assumed Parameters	
Temperature	1700C
Initial Particle Temperature	30C
Heat Transfer Coefficient	10000 W/m^2 K
Thermal Conductivity For Ni	60.7 W/m K
Radius of Particle	2.25 E-2 mm
Exit Velocity of Particle	30 m/s
Dynamic viscosity of air at 1700C	4.549 E-5 Ns/m^2
Flight time of vectored particle	3.7 E-3 s
Flight time of un-vectored particle	8.1 E-3 s
Vectored Particle Travel Distance	10.32 cm
Un-Vectored Particle Travel Distance	20.32 cm

The following governing equation for energy transfer in a sphere [16] was used to estimate the temperature distribution a Ni particle

$$\frac{\partial T}{\partial t} = \frac{\alpha}{r^2}\frac{\partial}{\partial r}\left(\frac{1}{r^2}\frac{\partial T}{\partial r}\right) \tag{7}$$

where $\alpha = k/(\rho c)$ is the thermal diffusivity of the particle, k is the thermal conductivity, ρ is the density and c is the specific heat. The assumptions for using this equation is that the particle is immersed in a large enough bath so that the energy transfer has minimal effect on the temperature of the bath. The boundary condition for the surface of the sphere was

$$k\frac{\partial T}{\partial t}|_{r=r_o} = h(T_\infty - T_s) \tag{8}$$

where h is the heat transfer coefficient, T_{\infty} is the temperature of the surrounding gas and T_s is the surface temperature of the particle. The initial condition was

$$T(r,0) = T_i \tag{9}$$

where T_i is the initial uniform temperature of the particle.

An analytical solution to the governing equation for temperature distribution that was provided by the *Fundamentals of Heat and Mass Transfer* [16] textbook is the following infinite series:

$$\theta^* = \sum_{n=1}^{\infty} C_n e^{\left(-\zeta_n{}^2 \mathrm{Fo}\right)} \frac{1}{\zeta_n r^*} \sin(\zeta_n r^*) \tag{10}$$

$$C_n = \frac{4[\sin(\zeta_n) - \zeta_n \cos(\zeta_n)]}{2\zeta_n - \sin(2\zeta_n)} \tag{11}$$

The $\zeta_n{}'s$ are the positive roots of

$$1 - \zeta_n \cot(\zeta_n) = \mathrm{Bi} \tag{12}$$

The dimensionless terms are defined as

$$\theta^* = \frac{T - T_\infty}{T_i - T_\infty}, \qquad r^* = \frac{r}{r_o}, \qquad \mathrm{Fo} = \frac{\alpha t}{r_o^2}, \qquad \mathrm{Bi} = \frac{h r_o}{k} \tag{13}$$

where r_o is the radius of the particle, Fo is the Fourier number and Bi is the Biot number.

The equation for the estimated flight times for the vectored and unvectored processes were derived from the following equation of motion for a sphere undergoing drag.

$$m\ddot{x} + b\dot{x} = 0 \tag{14}$$

The estimated flight times were calculated from the following equation

$$t = \frac{m_p}{b} \ln\left(\frac{1}{1-\frac{bx}{m_p v_o}}\right) \tag{15}$$

where m_p is the average mass of a particle of Ni based upon material specifications, $b = 6\pi\mu r_o$ is the drag coefficient for a sphere with very low velocity (Re < 1) according to Stoke's law, μ is the dynamic viscosity at the assumed average gas temperature, x is the distance traveled by the particle and v_o is the assumed initial particle velocity. A Matlab solver written by Recktenwald [17] was used to find the roots of Equation 12 and calculate the temperature profile of a sphere immersed in a surrounding fluid of uniform temperature. 397 positive roots (ζ_n) were found for Equation 12.

The kinetic energy of a Ni particle was calculated using Equation 16.

$$T_{kin} = \frac{1}{2} m_p \left(v_o - \frac{b}{m_p} x\right)^2 \tag{16}$$

Figure 32 shows the estimated temperature distributions for particles in the two different processes. The calculated kinetic energies for the vectored and un-vectored particles at impact are shown in Table 6.

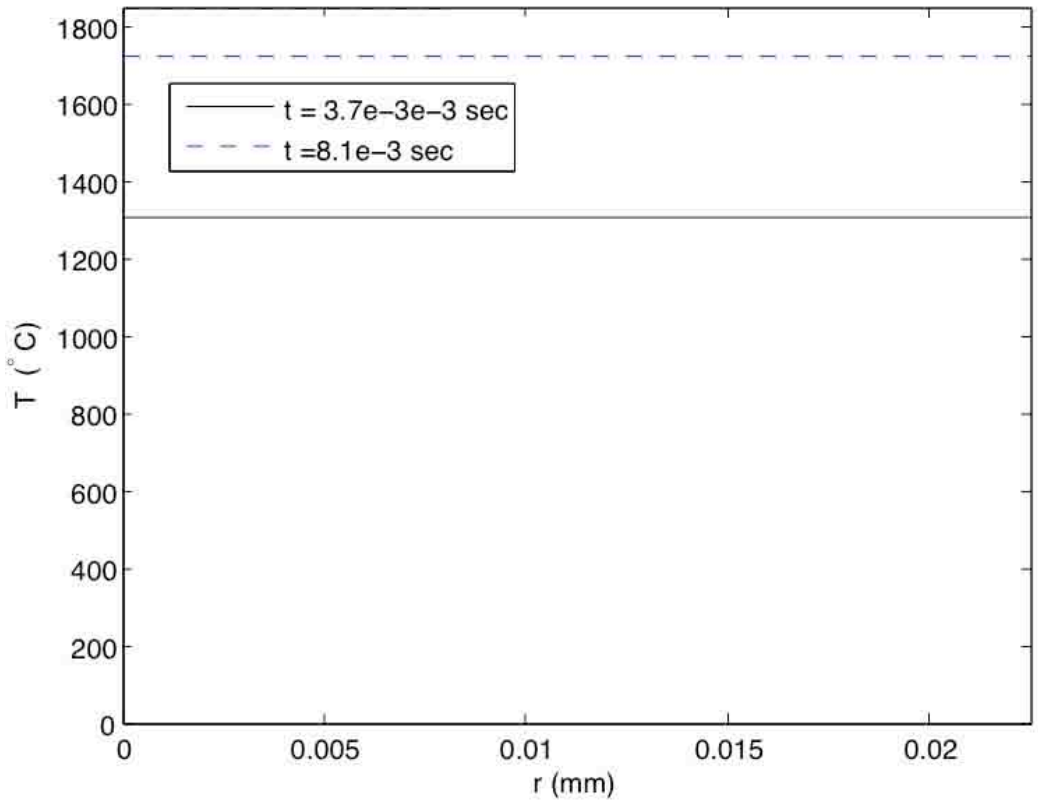

Figure 32 Time dependent temperature profile of vectored and un-vectored Ni particle spheres for h=10,000 W/m^2 K.

Table 6 Estimated Kinetic Energies

Estimated Kinetic Energy of the Particles at Impact	
Vectored	**Un-Vectored**
1.365 E-7 J	9.119 E-8 J

Testing Procedures

Porosity Measurement

Porosity measurements were conducted on samples 049-072. The measurement of porosity was based upon the Archimedes Principle Equation:

$$W_a + B - W = 0 \tag{17}$$

$$B = \rho_{water} \times V \times g \tag{18}$$

where W_a is the apparent weight of the coating in water, B is the buoyancy force acting on the coating, W is the actual weight of the coating. ρ_{water} is the density of water, V is the volume of the coating and g is the gravitational acceleration. The density of the coating was calculated from Equation 19

$$\rho_{coating} = \frac{M_{air}}{M_{air} - M_{water}} \times \rho_{water} \tag{19}$$

where M_{air} is the mass of the coating in air and M_{water} is the apparent mass of the coating in water. The percentage of porosity was found by calculating the percent of the difference between the density of cast Ni, ρ_{Ni}, and the density of the coating, $\rho_{coating}$, as shown in Equation 20.

$$\frac{\rho_{Ni} - \rho_{coating}}{\rho_{Ni}} \times 100 = \%\, of\ Porosity \tag{20}$$

The temperature of the water was approximately 23 C.

Surface Roughness and Profile Measurements

Surface roughness measurements were conducted on samples 049-072. Surface profile measurements were conducted on samples 050, 058, 061 and 072. The surface height was measured with the initial height set to zero for each sample. Three parallel measurements, 2.54 mm (0.1 in.) long and 6.35 mm (0.25 in.) apart, were measured for each sample in the Y direction of the coating surface. The travel speed was 0.102 mm/s (0.004 in/s). From these measurements the average surface roughness was calculated using Equation 21

$$R_a = \frac{1}{n}\sum_{i=1}^{n}|y_i| \quad (21)$$

where y_i is the measured deviation from the ideal surface at the ith point.

Microhardness Measurement

Microhardness measurements were conducted on samples 049-072. A Vickers hardness test was used to measure the microhardness at five locations per sample. The applied loading was 1 kgf for 10 seconds. Equation 22 was used to calculate the microhardness

$$HV = \frac{1.8544 \times 1kgf}{d^2} \quad (22)$$

where *d* was the average length of the two diagonals measured and had units of mm.

Tensile Strength Measurement

Tensile strength measurements were conducted on samples 001-048.Tensile strength measurements were performed according to ASTM C633 standard.

CHAPTER 5

RESULTS AND DISCUSSION

Porosity Measurement

Figure 33 and Figure 34 display the results of the porosity measurements for the vectored and un-vectored processes at spray angles ranging from 90° - 45° for samples 049-072. In Figure 33 the trend line of the data has a general upward slope for spray angles from 90° - 60° and then jumps down at 45°. In Figure 34 the trend line of the data has a general downward slope for spray angles from 90° - 45°. The size of the scatter-band from one spray angle to the next is relatively similar within the same spray process. However, the size of the scatter-band is consistently higher for the samples from the vectored spray process.

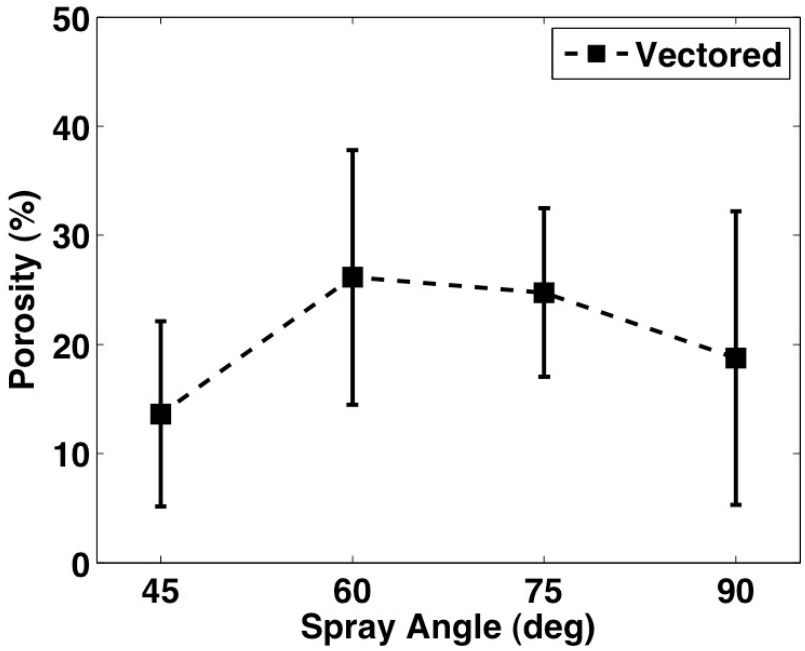

Figure 33 Vectored porosity test results.

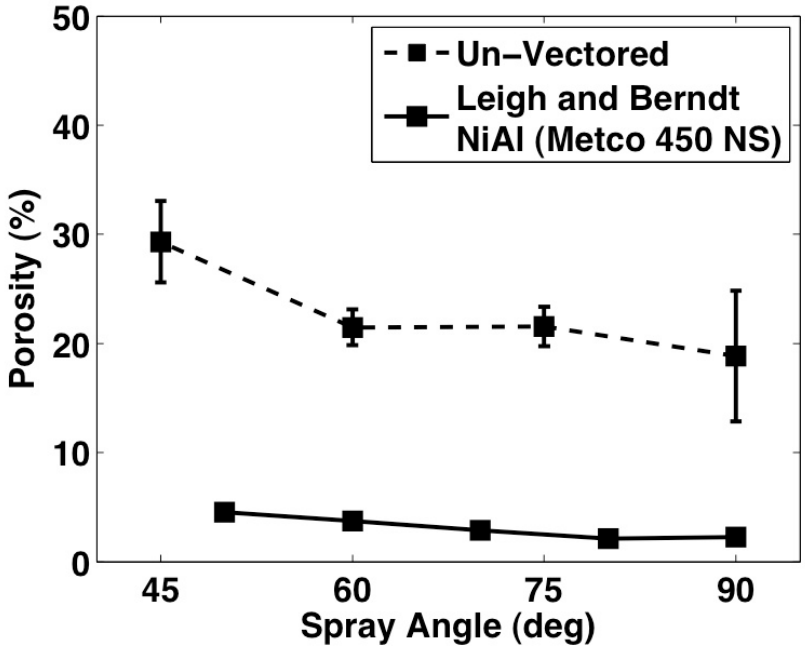

Figure 34 Un-vectored porosity test results.

The upward trend agreed well with previous results found by Montavon et al. [5], Smith et al. [10], Ilavsky et al. [12], Leigh et al. [11] and Tillman et al. [3] where the porosity was attributed to the shadow effect introduced by Kanouff et al. [7]. However, the downward jump at the 45° spray angle in the vectored process had not been seen before. The existence of this jump might indicate a unique feature of the vectored spray process. A possible cause for the jump in porosity could have been due to particles breaking asperities off. This in turn would have reduced the shadow effect, which likely decreased the chances for pore development. To support this idea, the kinetic energy of a Ni particle at impact for the vectored and un-vectored processes was calculated. The findings indicated a 33% increase in kinetic energy at impact for the particles of the vectored spray process. It was therefore likely that the particles sprayed at 45° for the vectored process surpassed a critical energy impact level that would break the asperity

formations of the surface coating. The particles sprayed at 45° for the un-vectored process were likely below this critical impact energy, and therefore, showed an increase in porosity.

The reason for the larger scatter-band for the measured porosity of the vectored spray process is not well known. It is possible that the that the shadow effect varied more during the vectored spray process which, in turn, would have increased the variation of porosity in the coatings. Variations in the shadow effect could have been due to the wider range of spray angles inherent with the vectored spray process as seen in Figure 35.

Another possible cause of the larger scatter-band could be due to larger particles randomly being vectored into the steeper spray angle regions of the spray cone. These particles could have randomly entered the primary flow of the at a greater *y* value that would have put it closer to the secondary flow (see Figure 5). Being closer to the flow would have given the larger particle a better chance to be vectored. The presence of these larger particles would have given rise to an increase in porosity. Their absence would have had the reverse effect.

Figure 35 Un-vectored and vectored spray cones. The top image shows the un-vectored spray cone. The bottom images show the vectored spray cone.

Surface Roughness Measurement

The surface roughness for sprayed particles using the vectored and un-vectored spray processes for spray angles of 90° - 45° can be seen in Figure 36 and Figure 37. The trend line for the vectored surface roughness test in Figure 36 indicates an increase in surface roughness for spray angles from 90° - 60° and then jumps down at 45°. The trend line for the un-vectored surface roughness test in Figure 37 indicates an increase in surface roughness from 90° to 75°, but a leveling off of the surface roughness for spray angles from 75° - 45°. Figure 36 and Figure 37 both show similar uncertainty levels for each of the spray angles for both processes. A correlation can be seen between the surface roughness and the material porosity for the vectored spray processes shown in Figure 36 and Figure 37, particularly for the 45° spray angle. A similarly strong correlation is not found for the un-vectored process.

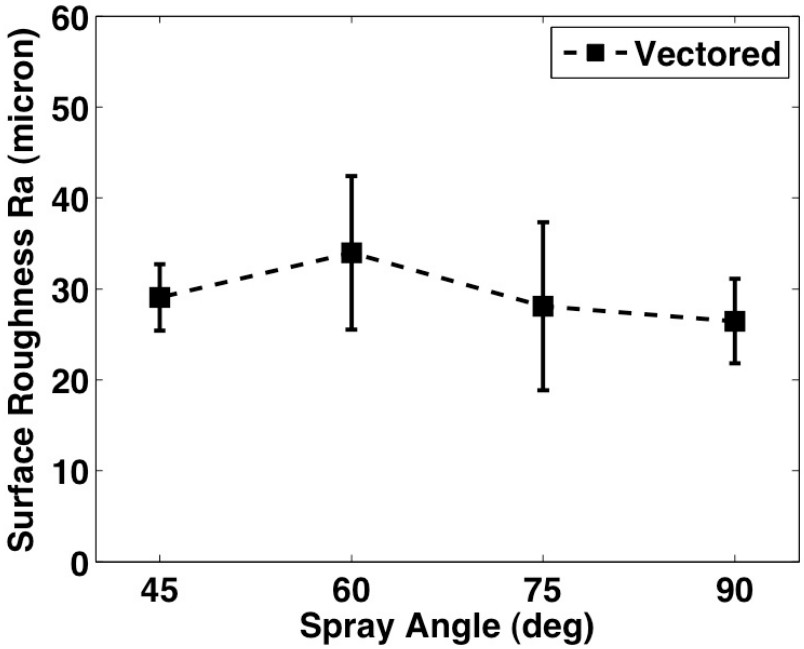

Figure 36 Vectored surface roughness test results.

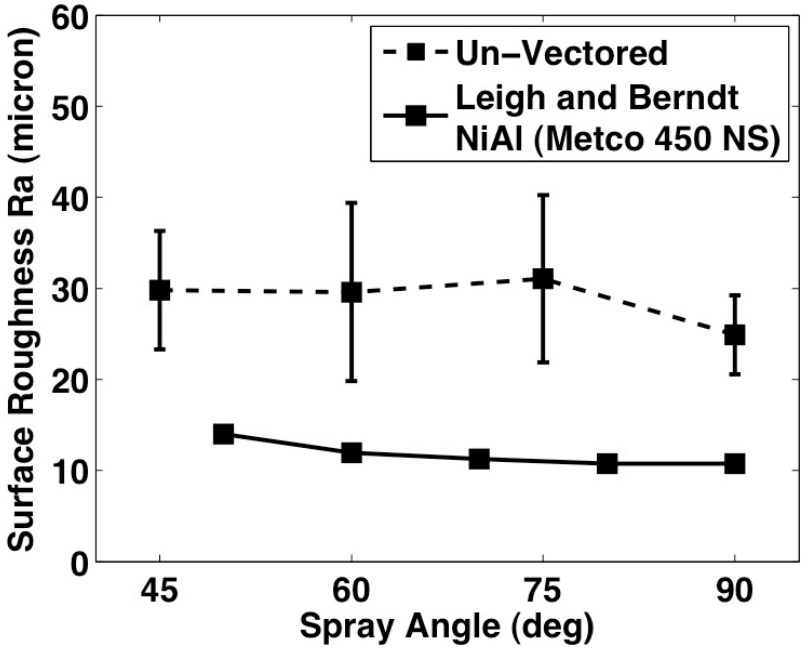

Figure 37 Un-vectored surface roughness test results.

The increase in surface roughness for the vectored spray process for the spray angles of 90° - 60° and the un-vectored spray process for the angles of 90° - 75° is similar to the increases in surface roughness measured by Kanouff et al. [7], Leigh and Berndt [11], Smith et al. [10], and Tillmann et al. [3]. The most likely cause for this increase in surface roughness was due to the particles impacting primarily on the asperity formations on the coating surface. The lack of a distinct upward trend for the un-vectored spray process for the spray angles of 75° - 45° is not unprecedented (see Figures [fig:Surface-Roughness-Data-Plots-01]-[fig:Surface-Roughness-Data-Plots-03]). Some of the materials tested in these studies did not show a significant upward trend in surface roughness until after the 45°. This indicates that the surface roughness was more sensitive to the spray angle for the vectored spray process.

Like the porosity measurements, the reduction in surface roughness for the vectored spray process for the 45° spray angle is likely due to the energy of the particle being high enough at the time of impact to sheer the asperities being impacted. Similarly, a study performed by Houdkova et al. [14] found a distinct downward trend in surface roughness as the spray angle decreased for some materials (see Figure [fig:Surface-Roughness-Data-Plots-03]). They attributed this reverse correlation to the possibility that the low angled particles were actually shearing off the asperities forming on the coating surface.

Microhardness Measurement

Figure 38 and Figure 39 display the results of the microhardness measurements against the spray angle for both the vectored and un-vectored processes. It can be seen from the figures that in both processes the microhardness decreased as the spray angle

decreased. By comparison, it can also be seen that the average microhardness for the vectored sprays for each spray angle in Figure 38 was less than that of the average microhardness of the un-vectored sprays for the same angles in Figure 39.

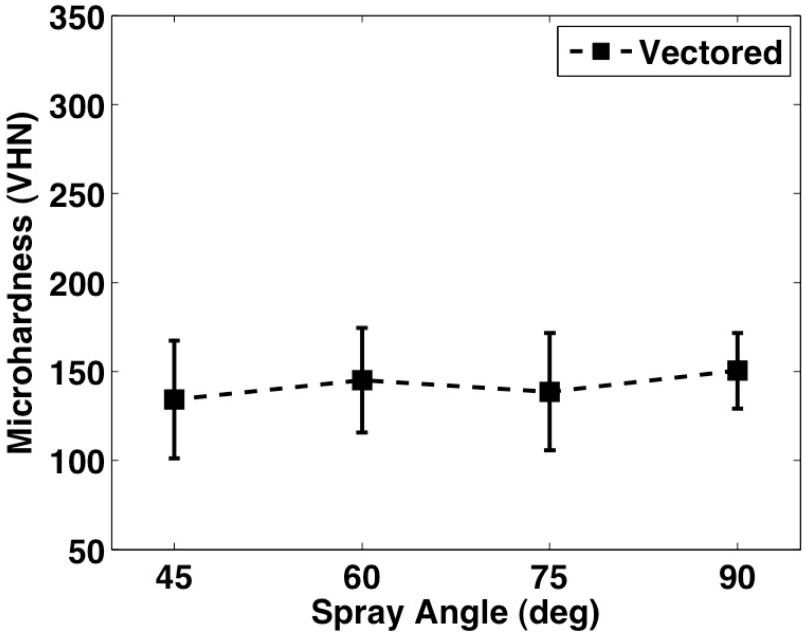

Figure 38 Vectored microhardness test results.

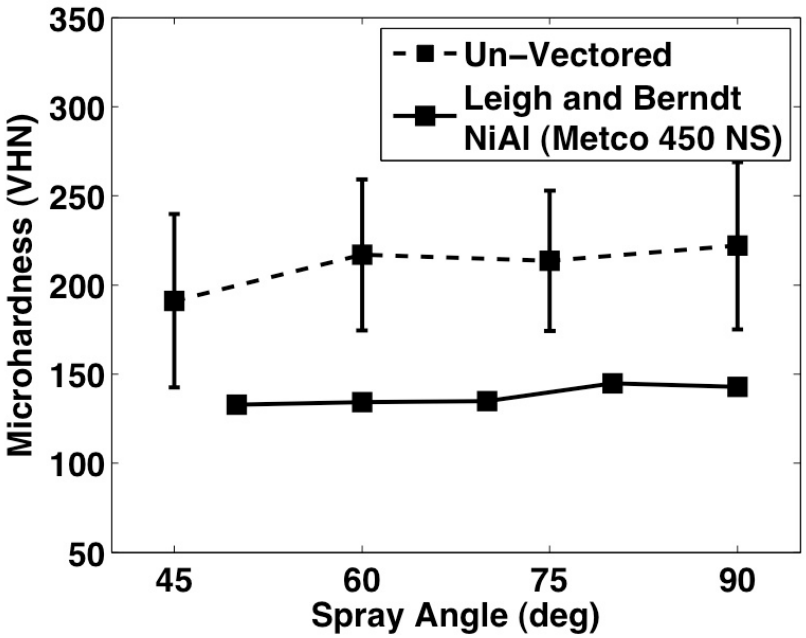

Figure 39 Un-vectored microhardness test results.

The decrease in microhardness as the spray angle decreased has been seen before by Leigh and Berndt [11], Strock et al. [13], and Houdkova et al. [14]. It was believed in their studies that the likely decrease in microhardness was due to an increase of porosity. Since hardness testing is a measurement of a material's ability to resist plastic indentation, it is likely that the hardness can be correlated to the material's porosity. This study also found that correlation between hardness and porosity.

The higher average microhardness for the un-vectored spray process could have been due to higher particle temperatures. Figure 32 displays the calculated time dependent temperature profiles versus the radius of a spherical particle at the estimated end time of flight for both the vectored and un-vectored spray processes. The heat transfer coefficient was unknown but estimated to be in the range between 2000-20,000 W/m^2 K. Other assumptions are recorded in Table 5. The resulting temperatures

appeared to be uniform throughout the entire radius of the particles. This was likely due to the high surface-to-volume ratio of the particle and the high thermal conductivity of Nickel even though the heating times are on the magnitude of milliseconds.

Figure 32 shows that the higher uniform temperature is that of the un-vectored particle. It should be noted here that the melting point of Ni is 15 C, which would indicate in this case that un-vectored particles would likely be in a liquid state whereas the vectored particles would likely be in a semi-liquidous state. The uniform temperature of the vectored Ni particle always remains substantially less than the un-vectored Ni particle for the range of heat transfer coefficients used. The findings from the time dependent temperature profile calculations indicate that the temperature of the un-vectored particles were higher than the vectored particles upon impact. This would have lead to better metallurgical bonding for the un-vectored coatings. Therefore, the higher densities found in Figure 39 are most likely due to a greater amount of metallurgical bonding between splats.

Sampath et al. [18] performed a study using three different coating techniques: wire arc, APS, HVOF and cold spray. In their experiment, the microhardness was measured against the particle's kinetic energy for each spray technique. Their results can be seen in Figure 40 which plots the average microhardness of NiAl coating against the kinetic energy/mole for each spray technique. The HVOF process achieved the highest hardness, which was the highest kinetic energy/mole process of the three thermal spray processes. Although the cold spray process sprayed particles had the highest energy of all four processes its microhardness performance was lower than that of HVOF. It was believed that the lower hardness was due to the non-metallurgical bonding associated

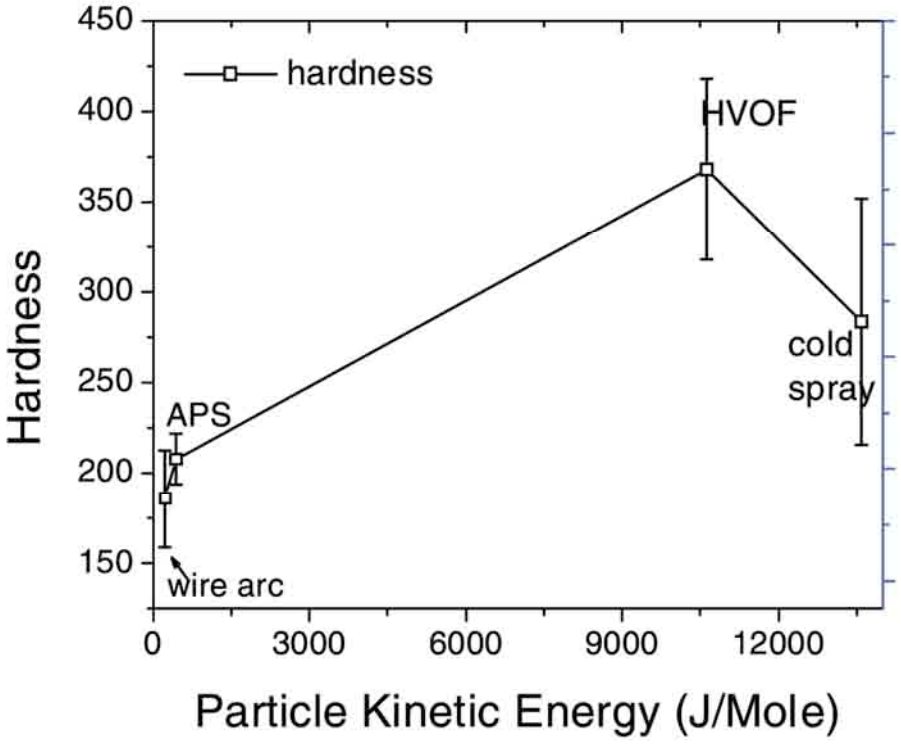

Figure 40 Sampath microhardness study [18].

with the cold spray process. Similarly, the particles of the vectored process had a higher kinetic energy at impact, but showcased a lower microhardness. This comparison also supports the theory that the higher microhardness of the un-vectored coatings was due to metallurgical bonding.

Tensile Strength Measurement

The tensile strength test was performed to showcase the tensile strength of the NiAl coating material. Two different thicknesses, T1 and T2, were sprayed for the vectored and un-vectored spray processes for spray angles of 90° - 45°. However, each of the samples failed at the bonding location of the coating/substrate interface between the NiAl coatings and the 1018 steel coupons. Therefore, Figure 41 and Figure 42 showcase

the tensile strength of the bond at the coating/substrate interface for the vectored and un-vectored processes for the spray angles of 90° - 45° for both thicknesses. Figure 41 shows that the bonding strength trend increased for the vectored process for spray angles of 90° - 45° for both thicknesses. Figure 42 shows that the bonding strength trend increased for the un-vectored process for spray angles of 90° - 45° for only the T2 thickness, but did not show any trend for the T1 thickness. Figure 42 shows that the overall average bond strength of the vectored process for both thicknesses was higher than the average bond strength of the un-vectored process for both thicknesses. The bond strengths decreased 37% and 43% from the vectored process to the un-vectored process for thicknesses T1 and T2, respectively.

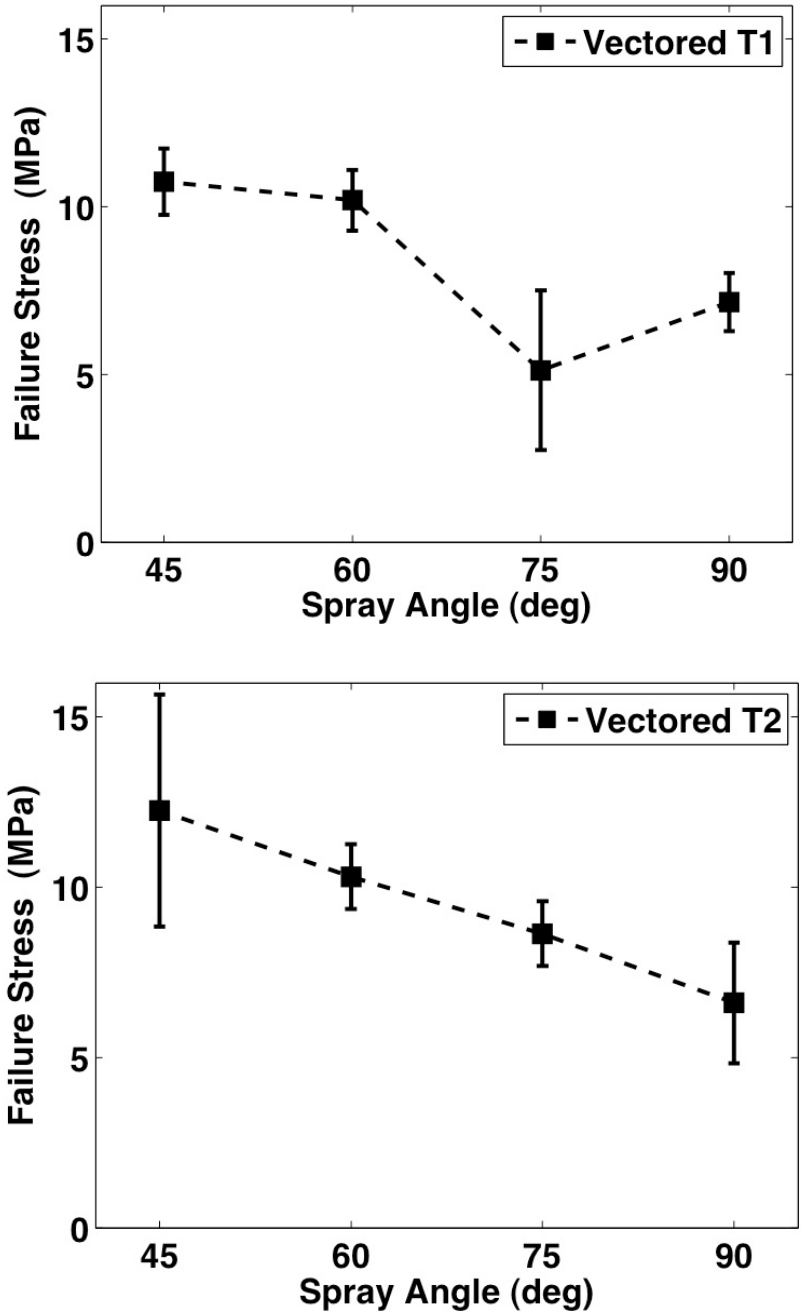

Figure 41 Vectored tensile strength test results.

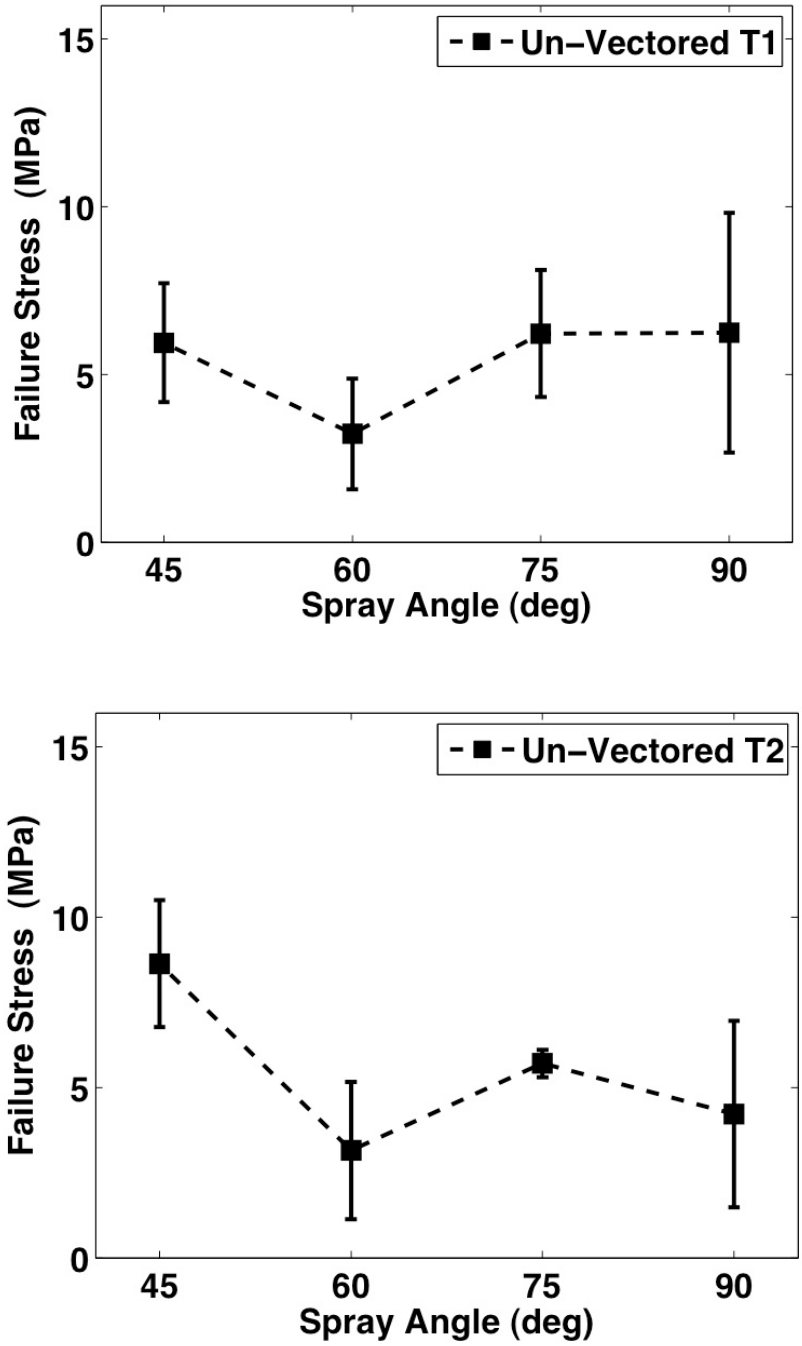

Figure 42 Un-vectored tensile strength test results.

Because the tensile test showcased bond failure at the coating/substrate interface these results could not be compared to the discussion of coating tensile strengths found earlier in this paper. However, an explanation of the measured results will be discussed. One reason for the change in the average bond strength between the two thicknesses could be due to the difference in kinetic energy of the initially sprayed particles at the time of substrate impact. The impact kinetic energies of the initially sprayed particles were different because the samples for the vectored spray process had to be moved closer to the gun in order to keep isothermic uniformity at the substrate surface. The approximate energies were calculated under the assumptions provided in Table 5. The calculated energy for the particles sprayed in the vectored process was approximately 33% higher than the particles sprayed in the un-vectored process, which corresponds with the change in the average tensile strengths between the two processes. It is therefore likely that the higher energy at impact allowed for better mechanical bonding at the coating/substrate interface dispute the higher viscosity of the vectored particles.

The increase in tensile strength measured as the spray angle decreased for both thicknesses of the vectored process and for the T2 thickness of the un-vectored process is surprising. No study has shown this type of trend before. One possible reason for this phenomenon could be that the substrate surfaces were in fact not uniform in surface roughness. If this were the case, then the coupons for the lower spray angles would have to have been randomly selected with increasingly rougher surfaces to produce the measured results. Figure 43 displays the surface profiles of three different 1018 steel coupons taken at random locations. These samples were machined using a lathe at the same cutting speed and depth. Figure 43 showcases that different areas of the profile of

the substrate surface have different levels of roughness within the same sample. These images indicate that the surface roughness were most likely the same.

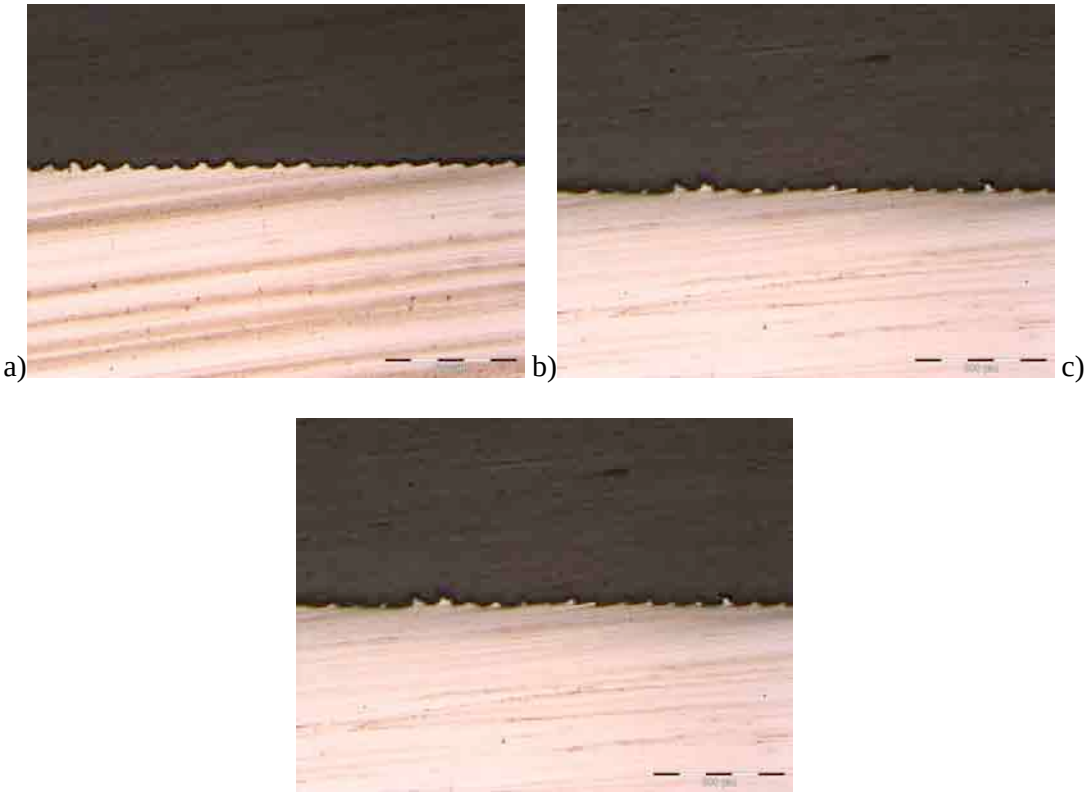

Figure 43 The surface roughnesses of the substrate surface. These images indicate that they were approximately the same. Both rough and smooth surface features were found randomly dispersed across the surface. It was unlikely that the coupons were randomly picked with increasingly larger surface roughness.

Another possible reason for the increased bond strength is that the lower angle sprayed particles in both processes gouged into the substrate surface upon impact. This would have allowed for better mechanical bonding as well, although there is no data to confirm this.

Microscopy

Figure 44 - Figure 47 display side by side comparisons of the vertical cross-

sections for the vectored and un-vectored process for spray angles from 90° - 45°. The following observations were made from the figures between the vectored and un-vectored processes. Figure 44 - Figure 47

- Show that for all spray angles the vectored splats appeared to be more spherical than the un-vectored splats. The spherical feature shows the un-melted particle shape.
- Show that the intersplat boundaries appear to be at a steeper angle for the vectored splats at 45º than for the un-vectored splats.

a)  b) 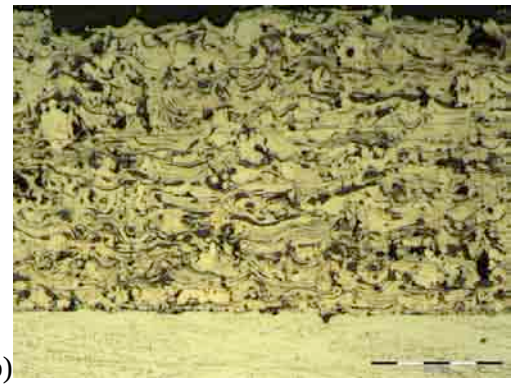

Figure 44 Microscopy images showing the splat formations for the vectored a) and un-vectored b) processes for the 90º spray angle.

a) 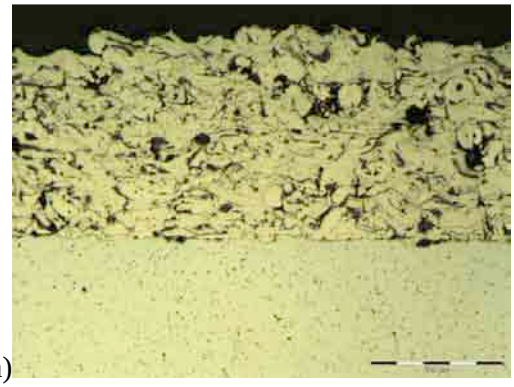 b) 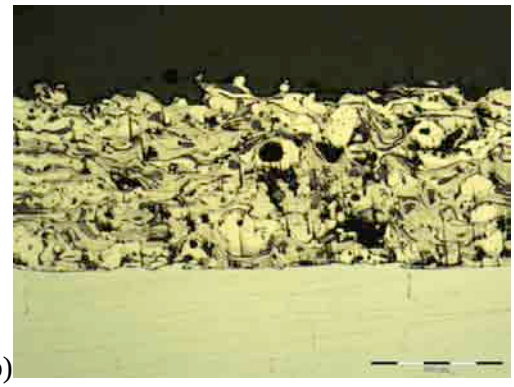

Figure 45 Microscopy images showing the splat formations for the vectored a) and un-vectored b) processes for the 75º spray angle.

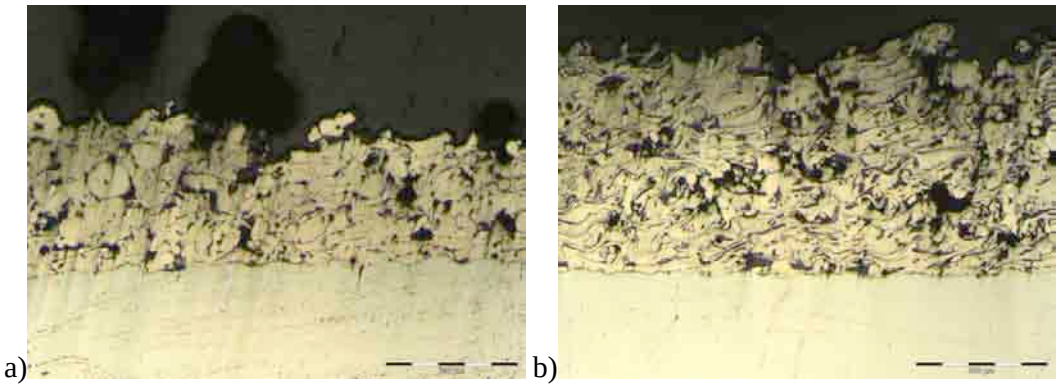

Figure 46 Microscopy images showing the splat formations for the vectored a) and un-vectored b) processes for the 60º spray angle.

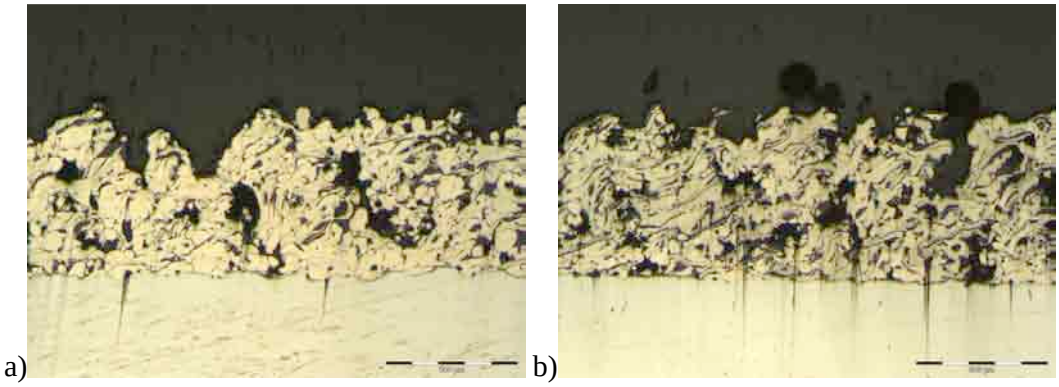

Figure 47 Microscopy images showing the splat formations for the vectored a) and un-vectored b) processes for the 45º spray angle.

The more spherical splat shapes in the vectored process were likely because the vectored splats were more viscous than the un-vectored splats upon impact. This would have been due to the shorter travel time in the flame for the particles in the vectored spray process which in turn was the reason for the lower calculated temperature distribution as seen in Figure 32. The higher viscosity on impact would have caused the particles to more likely retain their spherical shape.

The most likely cause of the steeper angle for the vectored splats at 45° was due

to the particles impacting at a steeper angle than the intended 45°. The spray of the vectored particles had an inherently larger spread than the un-vectored spray as seen in Figure 35. It is therefore likely that a greater percentage of particles would have impacted at a lower angle than the average angle of 45°.

The microscopy images also show several similarities between the vectored and un-vectored processes. Figure 44 - Figure 47

- Show that the intersplat boundaries for each spray angle tend to be perpendicular to the spray angle direction.
- Show that the intersplat boundaries are more jagged than the splat/substrate boundaries.
- Do not show a distinguishable difference in porosity by visual inspection.

The tendency of the intersplat boundaries to be perpendicular to the spray angle found in Figure 44 were likely due to the angle of impact of the sprayed particles and the resultant surface angle of the formed surface asperities. As the spray process continued these asperities would continue to build up in the direction perpendicular to their surface. In addition, this was probably the preferred crystallographic direction in the splat grains as suggested by Smith et al. [10].

The greater jaggedness between the intersplat boundaries than between the splat/substrate was probably due to the splashing and spreading of the particles upon impact. This splashing and spreading is evidenced by the flat splat formations found in Figure 44 - Figure 47. The splashing and spreading would have in turn allowed for greater mechanical bonding between the splats than between the initial splats and the substrate. This is evidence supporting the idea that the intersplat tensile strength was

much greater than the splat/substrate tensile strength and therefore the reason why the samples failed at the splat/substrate interface instead of in the intersplat interface.

The darkest spots in Figure 44 - Figure 47 indicate places of porosity.

CHAPTER 6

CONCLUSION

The effect of using a Coanda-Assisted Spray Manipulation collar on a combustion flame spray gun using NiAl powder has been studied. The use of the CSM collar resulted in the need to position the specimen approximately 50% closer to the gun. It also resulted in an approximately 33% decrease of the surface coating microhardness. The effect of moving the samples closer to the gun resulted in approximately 37% and 43% higher coating/substrate bond strength for the T1 and T2 thickness, respectively. No noticeable effect was made on the surface roughness, densities, or profiles by using the CSM. The results confirmed previous conclusions that density decreases, surface roughness increases and microhardness decreases as the spray angle decreases.

Future tests could be performed using different powder material and different types of flame spray guns. Further studies of the tensile strength of the coating should be done on coupons with rougher substrate surfaces to ensure that the mechanical bonding strength is higher than the intersplat bonding strength. This would ensure that measured tensile strengths indicated the tensile strength of just the coating material.

The use of the CSM collar can be used in the combustion flame spray process, but requires the gun to be positioned closer to the substrate surface. Use of the collar is also likely to decrease the microhardness of the material, but not significantly affect the material's porosity and surface roughness.

REFERENCES

[1] Davis, J., 2005, *Handbook of Thermal Spray Technology,* ASM International., Materials Park, OH, Chap. 1.

[2] England, G., 2010, “Thermal Spray Coatings,” Surface Engineering Forum www.gordonengland.co.uk/xtsc.htm.

[3] Tillmann, W., Vogli, E., and Krebs, B., 2008, “Influence of Spray Angle on the Characteristics of Atmospheric Plasma Sprayed Hard Material Based Coatings,” Journal of Thermal Spray, **17** (5-6), pp. 948-955.

[4] Allen, D., 2008, “Axisymmetric Coanda-Assisted Vectoring,” thesis, Utah State University, Logan, UT.

[5] Montavon, G., Coddet, C., Sampath, S., Herman, H., and Berndt, C., 1994, "Vacuum Plasma Spray Forming of Astroloy: An Investigation of Processing Parameters", "Proceedings of the 7th National Thermal Spray Conference", ASM International, Boston, MA., pp. 469-475.

[6] Madejski, J., 1976, “Solidification of Droplets on a Cold Surface,” International Journal of Heat and Mass Transfer, **19**, pp. 1009-1013.

[7] Kanouff, M., Neiser, R., and Roemer, T., 1998, “Surface Roughness of Thermal Spray Coatings Made with Off-Normal Spray Angles,” Journal of Thermal Spray Technology, **7**(5), pp. 219-228.

[8] Kang, C., and Ng, H., 2006, “Splat Morphology and Spreading Behaivor Due to Oblique Impact of Droplets Onto Substrates in Plasma Spray Coating Process,” Surface and Coatings Technology, **200**, pp. 5462-5477.

[9] Bussmann, S., Chandra, S., and Mostaghimi, J., 2000, “Numerical Results of Off-Angle Thermal Spray Particle Impact”, University of Toronto, Toronto, ON

[10] Smith, M., Neiser, R., and Dykhuizen, R.C., 1994, "An Investigation of the Effects of Droplet Impact Angle in Thermal Spray Deposition", "Proceedings of the 7th National Thermal Spray Conference", ASM International, Boston, MA., pp. 603-608.

[11] Leigh, S. H., and Berndt, C. C., 1997, “Evaluation of Off-Angle Thermal Spray,” Surface and Coatings Technology, **89**, pp. 213-224.

[12] Ilavsky, J., Allen, A. J., Long, G. G., Krueger, S., Berndt, C. C., and Herman, H., 1997, "Influence of Spray Angle on the Pore and Crack Microstructure of Plasma-Sprayed Deposits," Journal of the American Ceramic Society, **80**(3), pp. 733-742.

[13] Strock, E., Ruggiero, P., and Reynolds, D., 2001, "The Effect of Off-Angle Spraying on the Structure and Properties of HVOF WC/CoCr Coatings," Engelhard Corporation, East Windsor, CT.

[14] Houdkova, S., Kasparova, M., and Zahalka, F., 2010, "The Influence of Spraying Angle on Properties of HVOF Sprayed Hardmetal Coatings," Journal of Thermal Spray Technology, **19**(5), pp. 893-901.

[15] Bach, F., Mohwald, K., and Engl, L., 2006, "Rougness Enhancement of HVOF Spray MCrAlY Bond Coatings for Adhesion Improvement of Ceramic Top Layers," "Proceedings of the 2006 International Thermal Spray Conference: Science, Innovation, and Application", B. Marple and C. Moreau, eds., ASM International, Seattle, WA, pp. 649-654.

[16] Incropera, F. P., Dewitt, D. P., Bergman, T. L., and Lavine, A. S., 2007, *Fundamentals of Heat and Mass Transfer*, John Wiley and Sons, Hoboken, NJ.

[17] Recktenwald, G., 2006, "Transient, One-Dimensional Heat Conduction in a Convectively Cooled Sphere," Portland State University, Portland, OR.

[18] Sampath, S., Jiang, X., Matejicek, J., Prchlik, L., Kulkarni, A., and Vaidya, A., 2004, "Role of Thermal Spray Processing Method on the Microstructure, Residual Stress and Properties of Coatings: an Integrated Study for Ni–5 wt.% Al Bond Coats," Materials Science and Engineering, **A364**, pp. 216-231.

APPENDIX

Table 7 Porosity Methods

Author	Method	Equipment	Additional Notes
Montavon et al. 1997	Unknown		
Smith et al. 1994	Quantitative Image analysis of polished metallagraphic cross sections	Leco 300 metallagraphic/ Macintosh Quadra 800/ Dapple Image Analysis Software	
Ilavsky et al. 1997	Mercury- Intrusion Porosimetry (MIP) and Archimedean (water displacement) Porosimetry	NIST Cold Neutron Research Facility at the National Institute of Standards and Technology in Gaithersburg, MD	
Leigh and Berndt 1997	Optical Image Analysis	Omnimet® l, Buehler Ltd., Lake Bluff, Illinois	The samples were first polished. 10 frames were measured and then averaged for each sample
Strock et al. 2001	Unknown		
Tillmann et al. 2008	Optical Image Analysis	Zeiss, Axiovision 4.6 Image Processing Software	
Houdkova et al. 2009	Archimedean (water displacement) Density Measurement	Unknown	

Table 8 Surface Roughness Methods

Author	Method	Equipment	Additional Notes
Smith et al. 1994	Stylus Profilometer	Detak 8000 w/2.5µm stylus radius	Stylus Force: 30 mg; Traverse Rate: 740 µm/min; Four 1.0 cm long scans were performed in four different locations for each sample. Scan was centered on the vertical mid plane slightly above or below the horizontal mid plane.
Leigh and Berndt 1997	Stylus Profilometer	Surftest III (Mitutoyo MFG. Co. Ltd.)	Cut-off Value: 0.8 mm; Transverse Speed: 6 mm/s. Measurement range was 30 µm for NiAl and 10 µm for Cr_{2}C_{2}-NiCr.
Kanouff et al. 1998	Digitized Cross Section	Unknown	The samples were cut, then polished and then digitized.
Strock et al. 2001			
Tillmann et al. 2008	3D Surface Profilometer	Alicona, model Infinite Focus	
Houdkova et al. 2009			

Table 9 Hardness Methods

Author	Method	Loading	Equipment	Additional Information
Leigh and Berndt	Vickers Hardness Test	300 gf (NiA1) & 500 gf (Cr_{3}C_{2}NiCr)	Micromet II (Buehler Ltd., Lake Bluff, Illinois) hardness tester.	Load held for 15 s. Indentations were on center line. Indentations were separated a distance at least three times the indentation diagonal.
Montavon et al.	Vickers Hardness Test	300 g	Unknown	Unknown
Strock et al.	Vickers Hardness Test	300 g	Unknown	Unknown
Tillmann et al.	Vickers Hardness Test	0.1kp (0.981 N)	Leco,modelM-400	Load was held for 15 s
Houdkova et al.	HR15N & Vickers Hardness Test	300 g (VHN)	Unknown	The Rockwell HR15N method was used according to specifications ENISO6508-1.

Table 10 Tensile Strength Methods

Author	Method	Equipment	Additional Information
Leigh and Berndt 1997	Tensile Test	Unknown	ASTM C 633 testing method; The pull-off bar had an 8 (5/16) mm hole instead of a tapped hole. The pull-off bar was slightly longer (30.48 mm (1.2 in))
Tillmann et al. 2008	Tensile Test	Mohr & Federhoff	DIN EN582 testing method

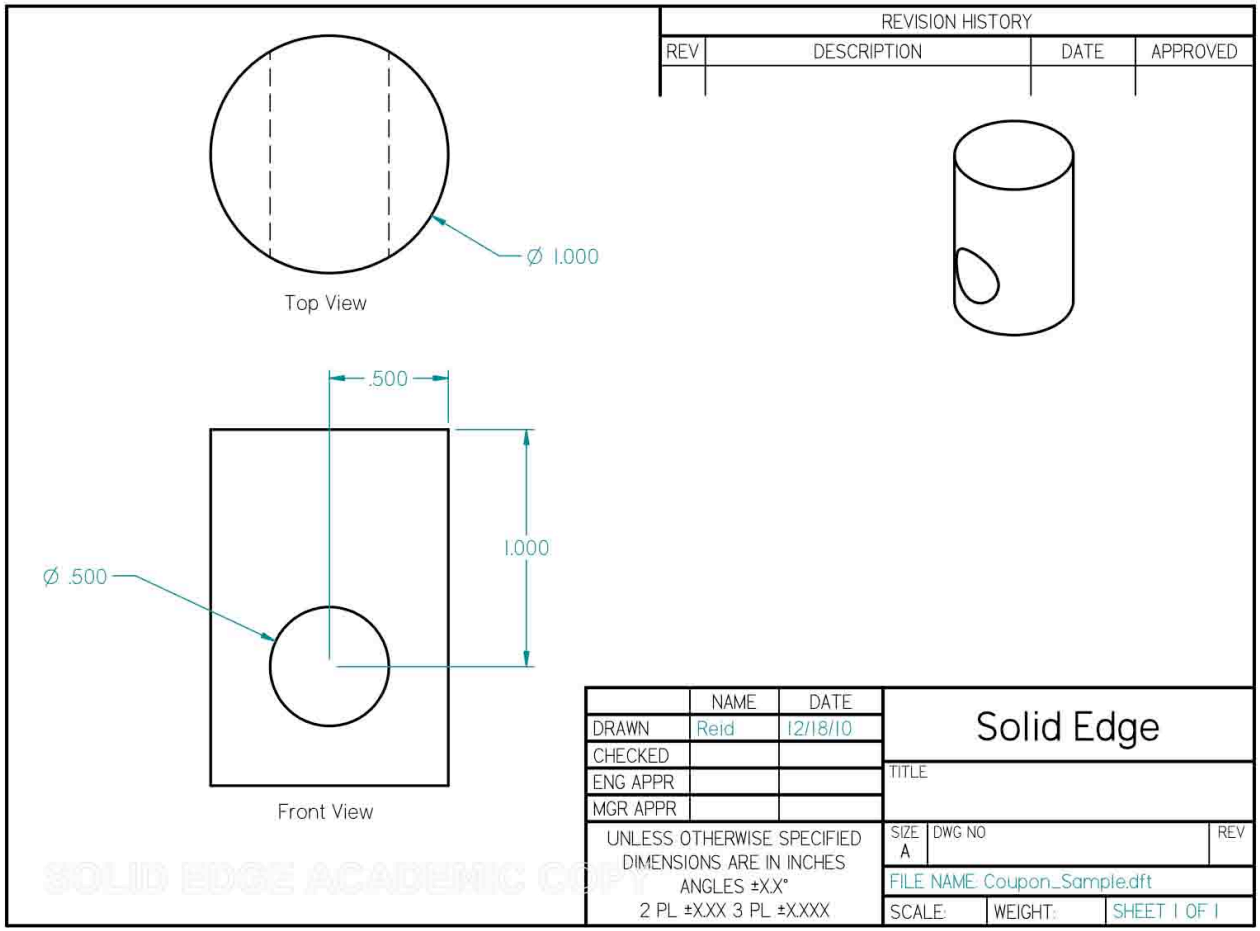

Figure 48 Coupon dimensions.

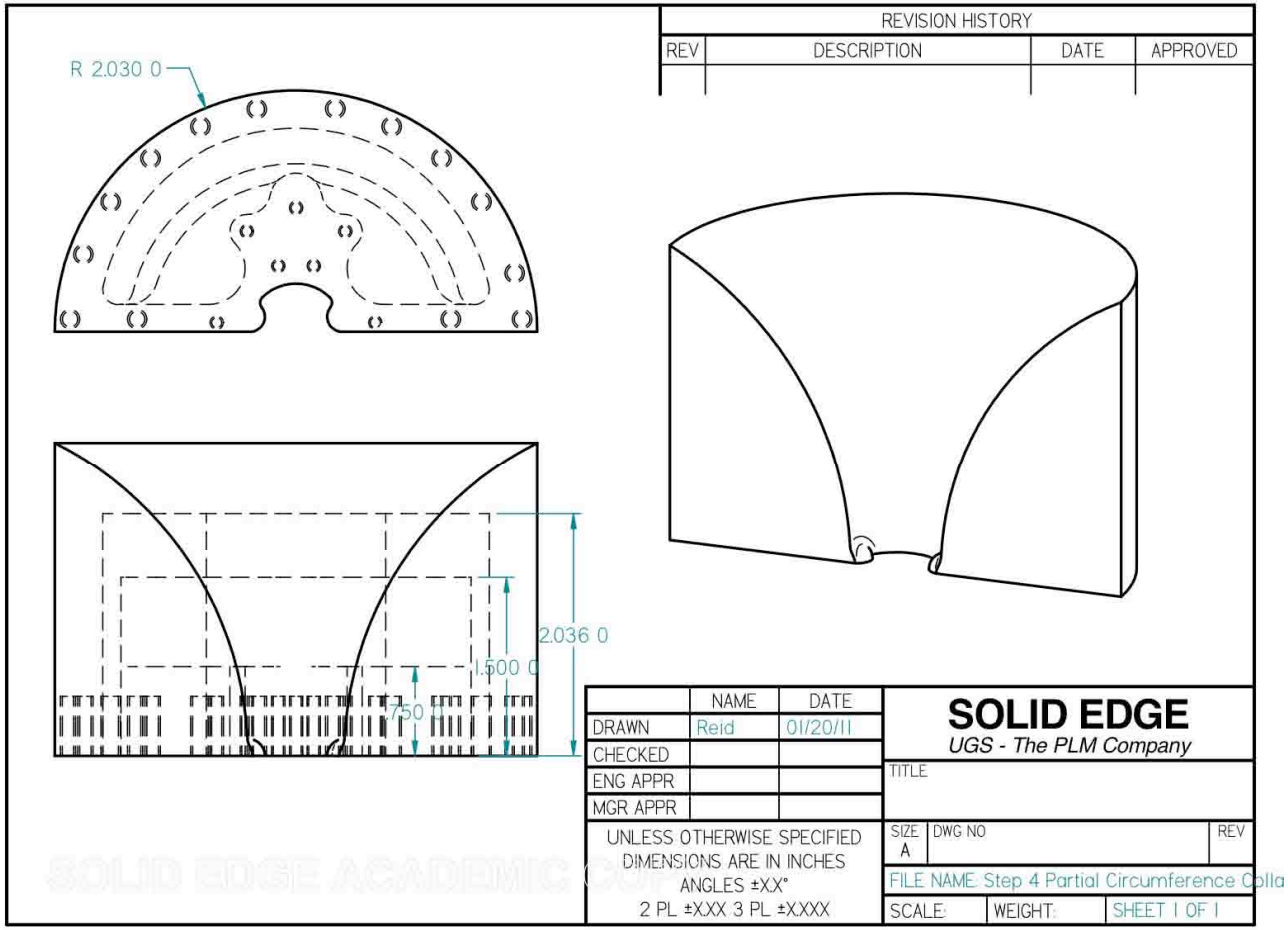

Figure 49 Partial circumference collar dimensions.

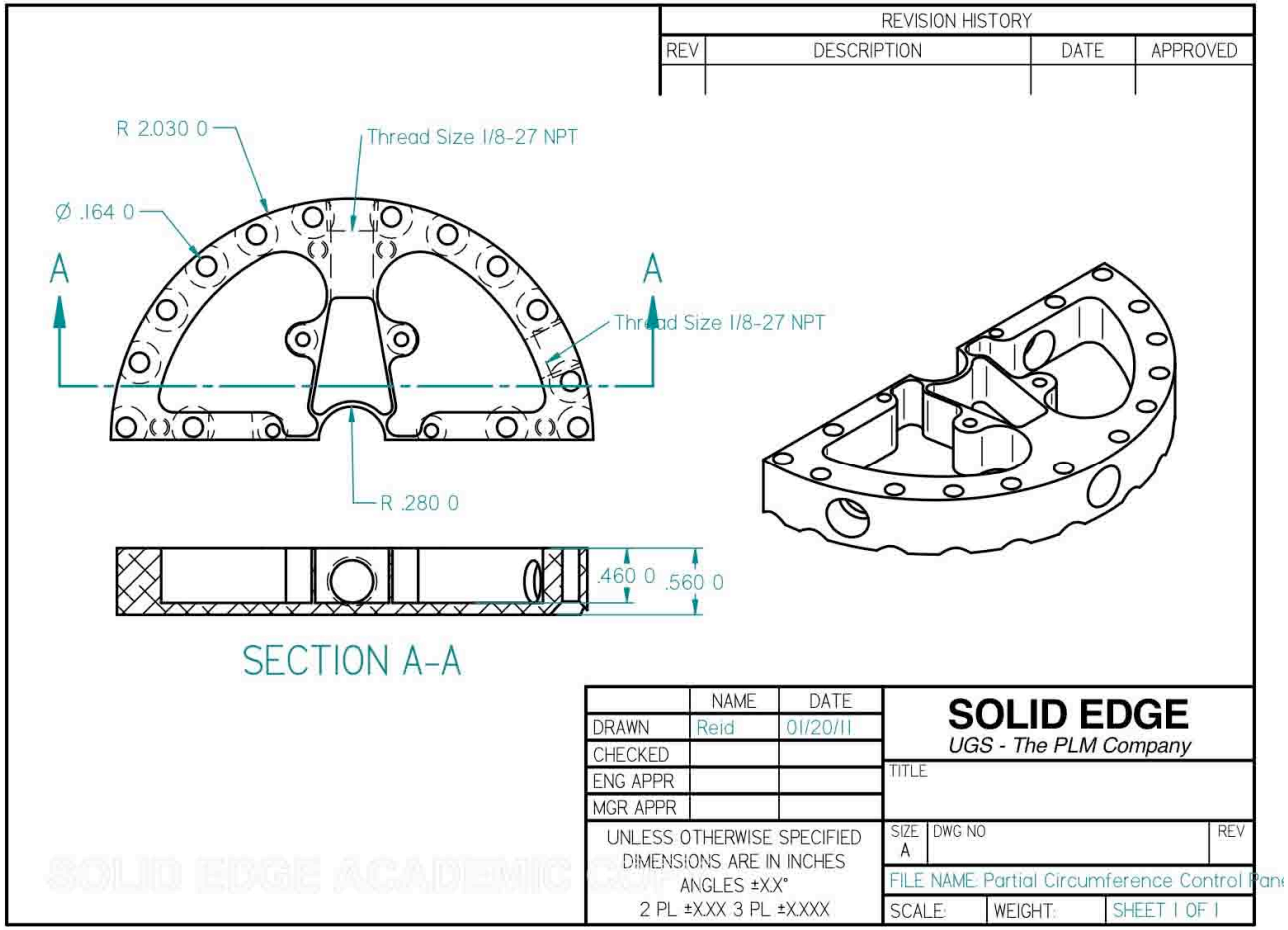

Figure 50 Partial circumference control panel dimensions.

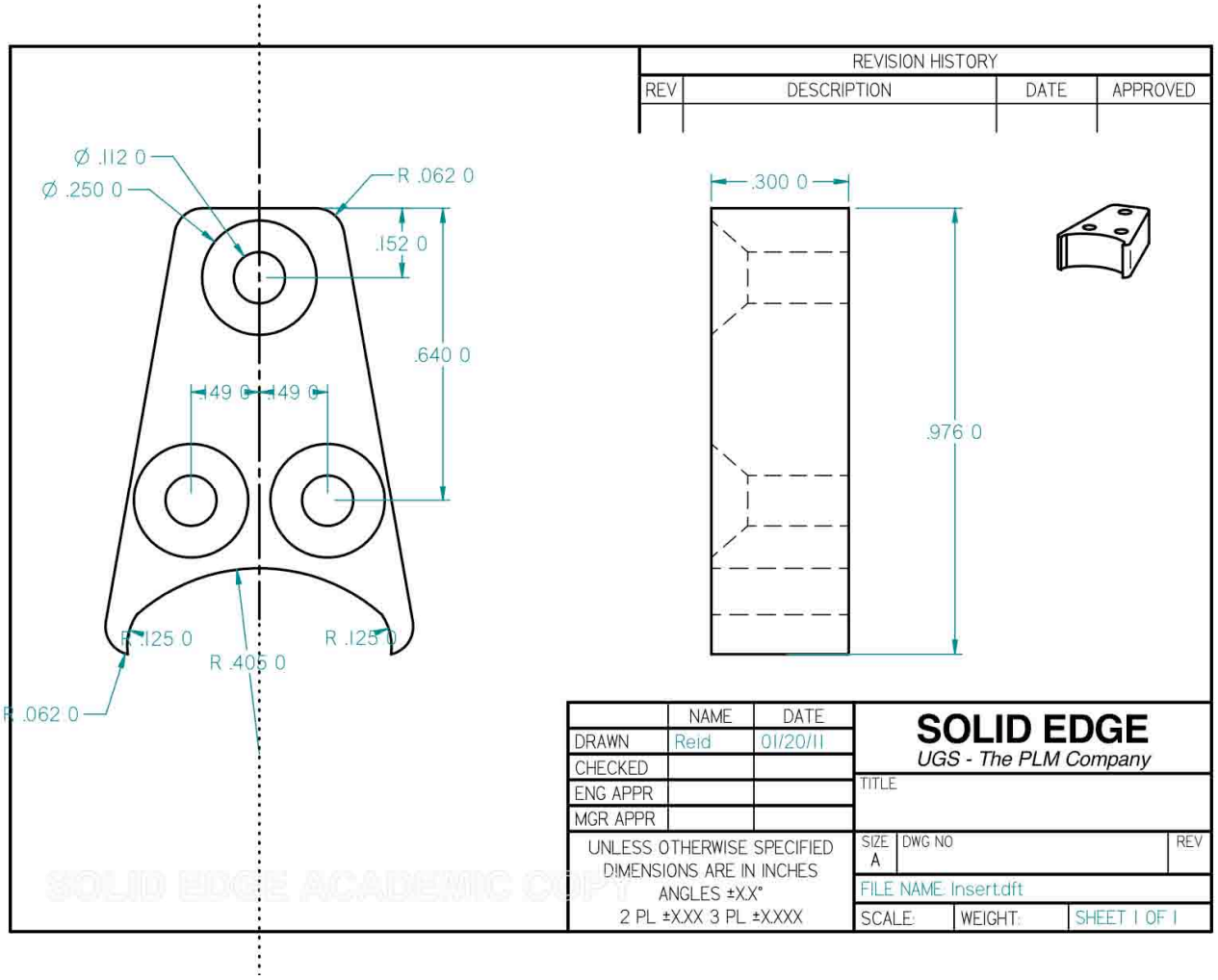

Figure 51 Insert dimensions.

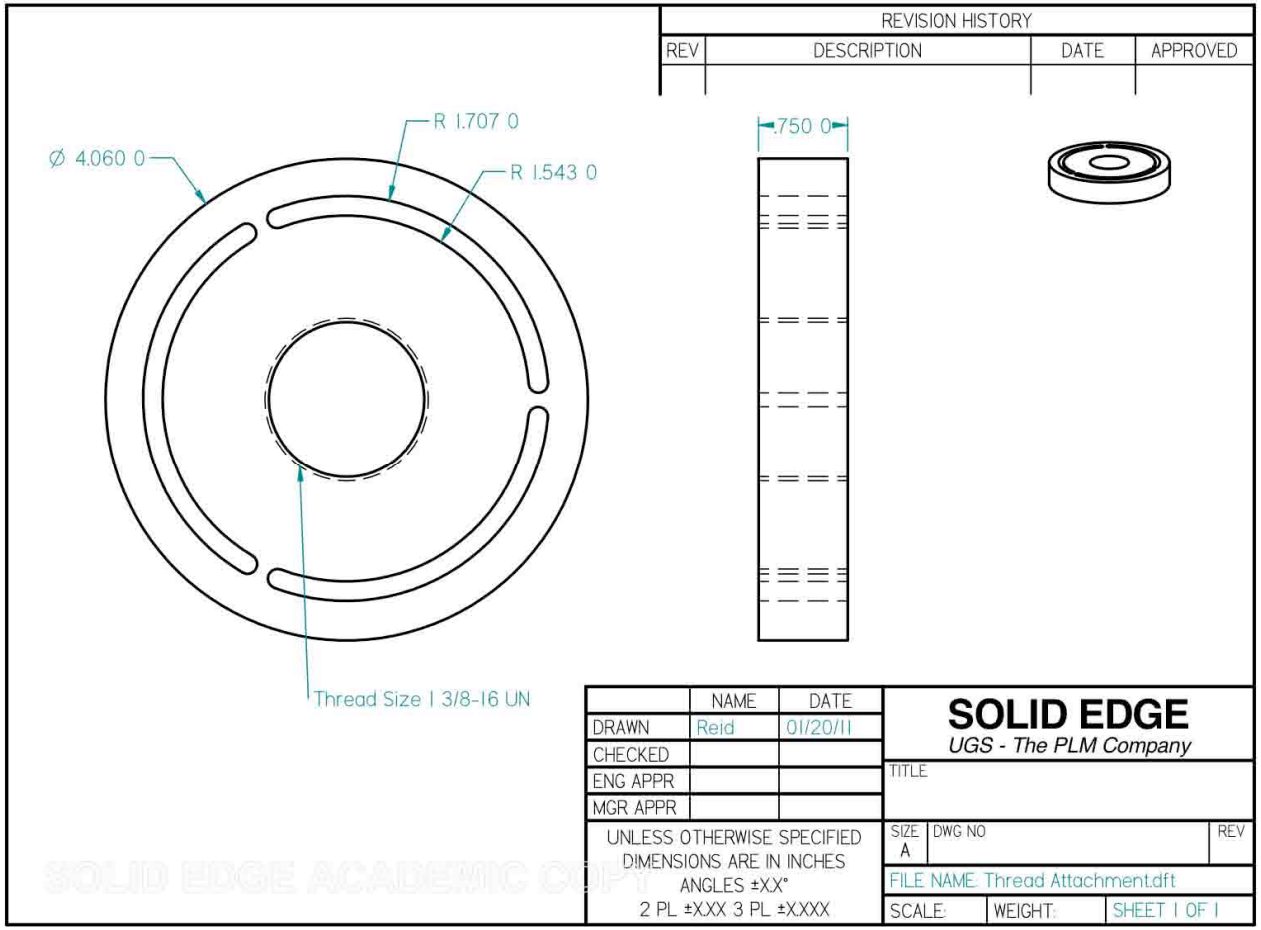

Figure 52 Thread attachment dimensions.